Energetic Constraints on Ocean Circulations of Icy Ocean Worlds

Malte F. Jansen[1], Wanying Kang[2] , Edwin S. Kite[1] , and Yaoxuan Zeng[1]
[1] Department of the Geophysical Sciences, The University of Chicago, Chicago, IL, USA; mfj@uchicago.edu
[2] Department of Earth, Atmospheric and Planetary Sciences, Massachusetts Institute of Technology, Cambridge, MA, USA
Received 2022 June 1; revised 2023 May 25; accepted 2023 May 30; published 2023 June 30

Abstract

Globally ice-covered oceans have been found on multiple moons in the solar system and may also have been a feature of Earth's past. However, relatively little is understood about the dynamics of these ice-covered oceans, which affect not only the physical environment but also any potential life and its detectability. A number of studies have simulated the circulation of icy-world oceans, but have come to seemingly widely different conclusions. To better understand and narrow down these diverging results, we discuss the energetic constraints for the circulation on ice-covered oceans, focusing in particular on Snowball Earth, Europa, and Enceladus. The energy input that can drive ocean circulation on ice-covered bodies can be associated with heat and salt fluxes at the boundaries as well as ocean tides and librations. We show that heating from the solid core balanced by heat loss through the ice sheet can drive an ocean circulation, but the resulting flows would be relatively weak and strongly affected by rotation. Salt fluxes associated with freezing and melting at the ice sheet boundary are unlikely to energetically drive a circulation, although they can shape the large-scale circulation when combined with turbulent mixing. Ocean tides and librations may provide an energy source for such turbulence, but the magnitude of this energy source remains highly uncertain for the icy moons, which poses a major obstacle to predicting the ocean dynamics of icy worlds and remains an important topic for future research.

Unified Astronomy Thesaurus concepts: Ocean planets (1151); Saturnian satellites (1427); Europa (2189); Hydrosphere (770); Planetary science (1255)

1. Introduction

Globally ice-covered oceans have been found on multiple moons in the solar system (Carr et al. 1998; Kivelson et al. 2000; Nimmo & Pappalardo 2016; Thomas et al. 2016) and spark our curiosity in part due to their potential to provide hospitable environments for life (Des Marais et al. 2008; Waite et al. 2017; Postberg et al. 2018; Hendrix et al. 2019). Earth's oceans may also have been covered by a global ice sheet during the so-called "Snowball Earth" events, and indeed eukaryotic life not only appears to have survived through these episodes, but may have evolved significantly during them (e.g., Hoffman et al. 2017). However, relatively little is known about these oceans beyond their existence, and due to our inability to directly observe them at present, we heavily rely on models to decipher their mysteries.

Although their potential biology may represent the holy grail for research on the icy-moon oceans, it is natural to start with the somewhat better-constrained problem of inferring the physical and chemical environment. In this study we specifically focus on the ocean circulation and mixing processes, which control the transport of heat and chemical tracers, including those that may affect life and our ability to observe its signatures (e.g., via material ejected in plumes).

Ocean circulation on icy moons can, broadly speaking, be driven by heat and salt fluxes, tidal forcing, or magnetic forces (e.g., Soderlund et al. 2020, and references therein). We here focus primarily on "buoyancy-driven" flows, i.e., flows associated with temperature and salinity gradients, although we also include a discussion about the role of tides and librations in driving vertical mixing, which in turn affects the buoyancy field and associated flow (e.g., Wunsch & Ferrari 2004). Following most of the previous work on buoyancy-driven flows, we will neglect magnetic forces, although they may be significant on Jupiter's moons (Gissinger & Petitdemange 2019).

A number of studies have simulated the buoyancy-driven dynamics of ice-covered oceans both in the context of Snowball Earth (e.g., Ashkenazy et al. 2013; Ashkenazy & Tziperman 2016; Jansen 2016) and icy moons (e.g., Soderlund et al. 2014; Soderlund 2019; Kang et al. 2020; Ashkenazy & Tziperman 2021; Zeng & Jansen 2021; Kang et al. 2022), and seem to have come to widely different conclusions, in particular with regards to the characteristic current speeds in these oceans. The Snowball Earth simulations of Ashkenazy et al. (2013), Ashkenazy & Tziperman (2016), and Jansen (2016) consistently show small-Rossby-number turbulent flows dominated by eddies and jets with characteristic velocities on the order of $1\,\mathrm{cm\,s^{-1}}$. For Europa, Soderlund et al. (2014) suggest moderate-Rossby-number convective turbulence. Soderlund et al. (2014) report results from their direct numerical simulation (DNS) in terms of nondimensional velocities (which amount to flow Rossby numbers) and find $|U/(2\Omega D)| \sim 0.5$. Taking these DNS results at face value and redimensionalizing with Europa's rotation rate and ocean depth[3] would suggest flow speeds in excess of $1\,\mathrm{m\,s^{-1}}$. Using a global circulation model for Europa's ocean, Ashkenazy & Tziperman (2016) instead find largely geostrophic (i.e., low-Rossby-number) turbulence and jets with characteristic velocities on the order of $1\,\mathrm{cm\,s^{-1}}$. In a parameter regime deemed applicable to Enceladus, DNS by Soderlund (2019) suggests $|U| \sim 0.1\,\mathrm{m\,s^{-1}}$ if the nondimensional velocities are taken at

---

---

[3] Using the rotation rate $\Omega \sim 2 \times 10^{-5}\,\mathrm{s^{-1}}$ and ocean depth $D \sim 1 \times 10^5\,\mathrm{m}$, $|U/(2\Omega D)| \sim 0.5$ translates to $|U| \sim 2.5\,\mathrm{m\,s^{-1}}$.

face value.[4] Instead Kang et al. (2020) and Zeng & Jansen (2021) find velocities on the order of 0.1 mm s^{-1} using global-scale ocean simulations. The flow dynamics and associated kinetic energy levels hence appear to vary widely across these studies, with variations across different studies being larger than variations between different oceans.

To shed some light on these apparent discrepancies and to establish what insights can be gained from first principles (i.e., without running numerical simulations whose results are sensitive to many parameters and assumptions), we here consider energetic constraints for the circulation of a globally ice-covered ocean. For simplicity we limit ourselves to an ocean in a statistical equilibrium state (as also assumed in all studies discussed in the previous paragraph). In particular, we assume that the net global ocean warming or cooling is small compared to the heat fluxes through the lower and upper ocean boundaries, and similarly that the net global mean freezing or melting rate is small compared to the regional rates. Nonequilibrium effects could be important (e.g., Hussmann & Spohn 2004; Nakajima et al. 2019), but would vastly widen the range of possible solutions. Our philosophy is that the better-constrained equilibrium problem should serve as a null hypothesis, which will be rejected if and only if evidence contradicts the assumptions or predictions of equilibrium ocean dynamics. Energetic constraints for equilibrium ocean dynamics allow us to put bounds on the expected circulation regimes and flow speeds, and to better understand seemingly diverging results from previous numerical simulations.

2. Energetics of the Seawater Boussinesq Equations

The weak compressibility of water allows us to employ the seawater Boussinesq approximation, with which the dynamical equations reduce to (e.g., Young 2010)

$$\frac{D\boldsymbol{v}}{Dt} + 2\boldsymbol{\Omega} \times \boldsymbol{v} + \nabla p = b\hat{k} + \mathcal{F}, \qquad (1)$$

$$\nabla \cdot \boldsymbol{v} = 0, \qquad (2)$$

where $\boldsymbol{v}$ is the velocity, $\boldsymbol{\Omega}$ is the planetary rotation, p is the pressure anomaly relative to a hydrostatic reference state with constant density, ρ_0, $b = g(\rho_0 - \rho)/\rho$ is the buoyancy[5] with g the gravitational acceleration, $\hat{k} = g^{-1}\nabla\phi$ is the normal vector in the direction of gravitational acceleration with ϕ the geopotential, and $\mathcal{F} = \mathcal{T} - \mathcal{D}$ is the acceleration due to tidal $\mathcal{T}$ and frictional $\mathcal{D}$ forces (where we define the frictional force with a negative sign for illustrative purposes, as it dominantly acts to decelerate the flow).

Multiplying Equation (1) by $\boldsymbol{v}$ and using $\nabla \cdot \boldsymbol{v} = 0$ yields an equation for the kinetic energy:

$$\frac{1}{2}\frac{D|\boldsymbol{v}|^2}{Dt} + \nabla \cdot (\boldsymbol{v}p) = wb + \boldsymbol{v} \cdot \mathcal{T} - \boldsymbol{v} \cdot \mathcal{D}, \qquad (3)$$

where w is the velocity normal to the geopotential surfaces (in practice usually well approximated by the radial velocity).

Integrating globally over the entire ocean volume and assuming an equilibrium state and no-normal-flow boundary conditions,[6] we find a balance between the conversion from potential to kinetic energy, wb, kinetic energy (KE) generation by tidal forcing, $\boldsymbol{v} \cdot \mathcal{T}$, and frictional dissipation, $\boldsymbol{v} \cdot \mathcal{D}$:

$$\int wb dV + \int \boldsymbol{v} \cdot \mathcal{T} dV = \int \boldsymbol{v} \cdot \mathcal{D} dV. \qquad (4)$$

We hence have two potential sources of kinetic energy: (1) the vertical buoyancy flux, which converts potential to kinetic energy and is directly related to the vertical heat and salt flux, and (2) tidal forcing. This paper will focus primarily on buoyancy-driven circulations; we assume a balance between the first term on the left-hand side (lhs) of Equation (4) and the dissipation on the rhs (see also Equation (3.2) in Paparella & Young 2002). The potential role of tides in modulating the buoyancy-driven circulation will also be discussed.

Importantly, Equation (4) highlights that buoyancy forcing can energetically drive a circulation if and only if it is distributed such that the global mean advective buoyancy flux required to balance the forcing (minus any diffusive flux) is directed upward. Notice that there is an interesting discussion in the Earth ocean literature about the implications of this statement for a purely "buoyancy-driven" circulation (i.e., without any mechanical forcing) in an ocean (or experimental apparatus) where all heating and cooling is applied at the surface (e.g., Sandström 1908; Paparella & Young 2002; Wunsch & Ferrari 2004; Hughes & Griffiths 2008). Energetically speaking, the energy source needed to balance any dissipation in this so-called "horizontal-convection" problem must come from molecular diffusion (which can flux buoyancy downward to balance an upward buoyancy advection that generates KE). We will return to the potential role of molecular diffusion below.

2.1. Buoyancy Forcing

The upward buoyancy flux is related to the upward flux of heat or compositional buoyancy. In this manuscript we assume a water ocean with dissolved salts, such that compositional buoyancy effects are encapsulated by the salinity. In general we thus allow buoyancy to be some function of potential temperature, salinity, and geopotential height (e.g., Young 2010):

$$b = \tilde{b}(\Theta, S, z), \qquad (5)$$

where Θ is the potential temperature,[7] S is the salinity, and z is the depth relative to some reference geopotential height level. The temperature and salinity evolve according to

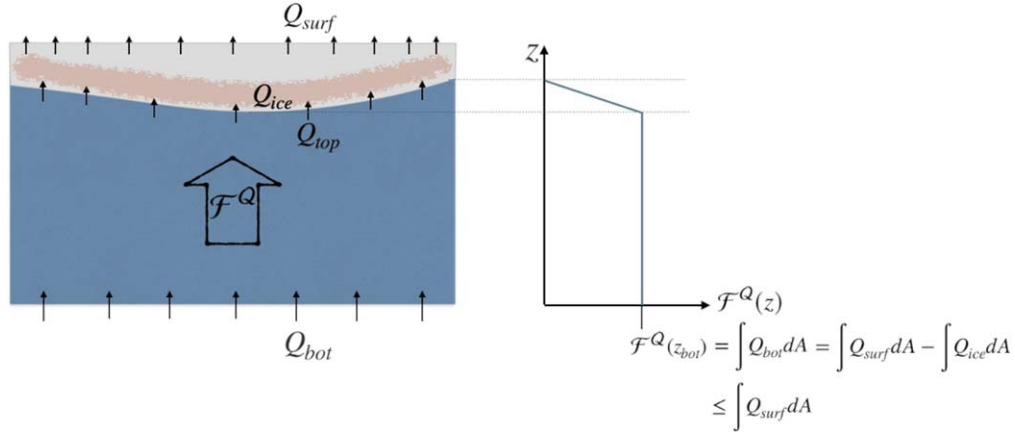$$\frac{D\Theta}{Dt} = \kappa_T \nabla^2 \Theta, \qquad (6)$$

Figure 1. Sketch of the vertical heat flux through the ocean, which provides the energy source for thermally driven flows. In this manuscript we assume that the ocean and ice sheet are in equilibrium, and that heat sources in the interior of the ocean are negligible, such that the globally integrated heat flux from the core ($\int Q_{\mathrm{bot}}dA$) is equal to the net globally integrated heat flux from the ocean to the ice sheet ($\int Q_{\mathrm{top}}dA$). Notice that the globally integrated vertical heat flux in the ocean ($\mathcal{F}^Q$) can also be constrained from the potentially more observable globally integrated heat flux emanating from the planetary body's surface ($\int Q_{\mathrm{surf}}dA$), which is given by the sum of the core heating ($\int Q_{\mathrm{bot}}dA$) and the tidal energy dissipation in the ice layer ($\int Q_{\mathrm{ice}}dA$). In particular, the maximum globally integrated vertical heat flux in the ocean is limited to $\mathcal{F}^Q \leqslant \int Q_{\mathrm{surf}}dA$.
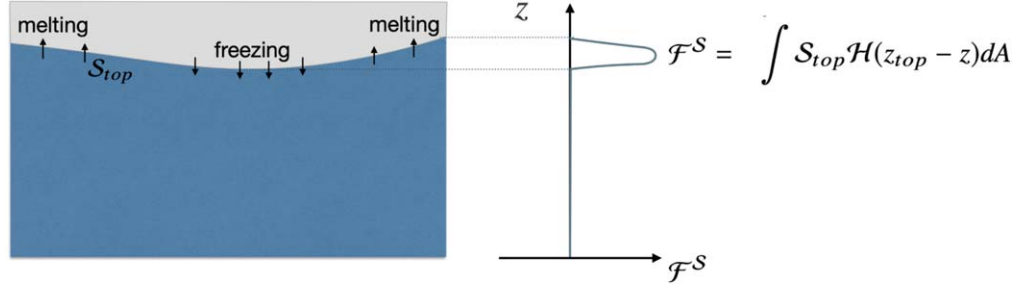

Figure 2. Sketch of the vertical salt flux through the ocean. If melting occurs under thinner ice and freezing occurs under thicker ice, as sketched here, the net globally integrated salt flux required in the ocean to balance brine rejection from freezing and melting ($\mathcal{F}^S$) is upward, which implies a downward buoyancy flux that converts kinetic to potential energy. In this scenario salt fluxes therefore do not energetically drive a circulation. Instead, kinetic energy from an alternative source is required to maintain a circulation that can flux salt upward.

$$\frac{DS}{Dt} = \kappa_S \nabla^2 S, \qquad (7)$$

with the boundary conditions

$$-\kappa_T \partial_z \Theta(z_{\mathrm{bot}}) = \frac{1}{\rho c_p} \mathcal{Q}_{\mathrm{bot}}, \quad -\kappa_T \partial_z \Theta(z_{\mathrm{top}}) = \frac{1}{\rho c_p} \mathcal{Q}_{\mathrm{top}}, \qquad (8)$$

$$-\kappa_S \partial_z S(z_{\mathrm{bot}}) = \mathcal{S}_{\mathrm{bot}}, \quad -\kappa_S \partial_z S(z_{\mathrm{top}}) = \mathcal{S}_{\mathrm{top}}, \qquad (9)$$

where κ_T and κ_S are the molecular diffusivities of heat and salt, respectively, and $\mathcal{Q}_{\mathrm{bot/top}}$ and $\mathcal{S}_{\mathrm{bot/top}}$ denote the heat and salt fluxes through the bottom and top boundaries, respectively. For simplicity we do not include significant heat sources in the interior, although such sources could be added.

If the equation of state is nonlinear, the conservation equations for Θ and S cannot be readily translated into a conservation equation for buoyancy. The most general way to account for nonlinearities in the equation of state, which is discussed in the Appendix, is to introduce the dynamic enthalpy, which is related to the potential energy. A significantly simpler (and more intuitive) result can be obtained if we assume that horizontal variations in the thermal and haline expansion coefficients are small, such that we can approximate

$$b \approx \langle b \rangle + \langle \alpha \rangle (\Theta - \langle \Theta \rangle) + \langle \beta \rangle (S - \langle S \rangle), \qquad (10)$$

where $\alpha \equiv g^{-1}\partial_\Theta b$ and $\beta \equiv g^{-1}\partial_S b$ are the thermal and haline expansion coefficients, respectively, and $\langle \cdot \rangle$ denotes a horizontal average at any given depth. Notice that α is typically positive (except for relatively fresh water at cold temperatures and modest pressures), while β, as defined here, is negative. We can then directly relate the total globally integrated upward advective buoyancy flux (which represents the source of kinetic energy in a buoyancy-driven flow) to the upward advective heat and salt fluxes:

$$\mathcal{B} \equiv \int wb\,dV \approx \int \left[g\langle\alpha\rangle \iint w\Theta\,dA \right] dz$$
$$+ \int \left[g\langle\beta\rangle \iint wS\,dA \right] dz \equiv \mathcal{B}^\Theta + \mathcal{B}^S, \qquad (11)$$

where we used that $\iint w\,dA = 0$ due to volume conservation, and we defined $\mathcal{B}^\Theta$ and $\mathcal{B}^S$ as the globally integrated net upward buoyancy fluxes associated with heat and salt advection, respectively.

The total upward heat and salt fluxes can be related to the sources and sinks of heat and salt via their conservation equations (see also sketches in Figures 1 and 2). In particular, the area-integrated vertical fluxes of heat and salt are constrained by the conservation of heat and salt above or below a respective level. In a statistically steady state, where the mean rate of change in Θ and S at any given depth is

approximately zero, Equation (6) can be integrated over the volume above or below some depth z to obtain an equation for the vertical buoyancy flux at this depth:

$$
\begin{aligned}
&\int (w\Theta - \kappa_T \partial_z \Theta) dA \\
&= \frac{1}{\rho c_p}\left[\int \mathcal{Q}_{\mathrm{bot}}\mathcal{H}(z - z_{\mathrm{bot}})dA - \int \mathcal{Q}_{\mathrm{top}}\mathcal{H}(z - z_{\mathrm{top}})\, dA\right] \\
&= \frac{1}{\rho c_p}\left[\int \mathcal{Q}_{\mathrm{top}}\mathcal{H}(z_{\mathrm{top}} - z)dA - \int \mathcal{Q}_{\mathrm{bot}}\mathcal{H}(z_{\mathrm{bot}} - z)\, dA\right] \\
&\equiv \frac{1}{\rho c_p}\mathcal{F}^{\mathcal{Q}},
\end{aligned}
$$

(12)

where $\mathcal{H}$ is the Heaviside function ($\mathcal{H}(x) = 0$ for $x < 0$ and $\mathcal{H}(x) = 1$ for $x > 0$), and we defined $\mathcal{F}^{\mathcal{Q}}$ as the the vertical heat flux across any depth z needed to balance the net heat and salt fluxes through the boundaries above and below the respective level. Similarly, Equation ((7)) can be integrated to obtain

$$
\begin{aligned}
&\int (wS - \kappa_S \partial_z S) dA \\
&= \int \mathcal{S}_{\mathrm{bot}}\mathcal{H}(z - z_{\mathrm{bot}})dA - \int \mathcal{S}_{\mathrm{top}}\mathcal{H}(z - z_{\mathrm{top}})\, dA \\
&= \int \mathcal{S}_{\mathrm{top}}\mathcal{H}(z_{\mathrm{top}} - z)dA - \int \mathcal{S}_{\mathrm{bot}}\mathcal{H}(z_{\mathrm{bot}} - z)\, dA \\
&\equiv \mathcal{F}^{\mathcal{S}}.
\end{aligned}
$$

(13)

Notice that interior sources of heat or salt could be included by modifying the definition of $\mathcal{F}^{\mathcal{Q}}$ and $\mathcal{F}^{\mathcal{S}}$, which generally need to balance any net sources or sinks above or below the respective level.

These definitions allow us to express the globally integrated KE generation associated with heat and salt flux forcing as:

$$
\mathcal{B}^{\Theta} \approx \underbrace{\int g\langle\alpha\rangle \frac{\mathcal{F}^{\mathcal{Q}}}{\rho c_p}dz}_{\mathcal{B}^{\Theta}_{\mathcal{F}}} + \underbrace{\int g\alpha\kappa_T \partial_z \theta dV}_{\mathcal{B}^{\Theta}_{\mathrm{diff}}},
$$

(14)

and

$$
\mathcal{B}^{S} = \underbrace{\int g\langle\beta\rangle \mathcal{F}^{\mathcal{S}}dz}_{\mathcal{B}^{S}_{\mathcal{F}}} + \underbrace{\int g\beta\kappa_S \partial_z S dV}_{\mathcal{B}^{S}_{\mathrm{diff}}}.
$$

(15)

The first term on the rhs of Equations (14) and (15) can be interpreted as the potential energy source associated with heat and salt forcing at the lower and upper boundaries, while the second term is the potential energy source or sink due to diffusion (which provides a source of mechanical energy whenever the stratification is statically stable, and a sink when it is unstable).

If vertical variations in $g\alpha$ and $g\beta$ are also small, thermal forcing at the boundaries provides a source of energy that can drive a circulation if, and only if,

$$
\alpha \int \mathcal{F}^{\mathcal{Q}}dz > 0,
$$

(16)

i.e., for $\alpha > 0$, heating, on average, needs to occur at a greater depth than cooling, while for $\alpha < 0$ cooling needs to occur at a greater depth than heating. Similarly, salt fluxes can drive

circulation only if

$$
\beta \int \mathcal{F}^{S}dV > 0.
$$

(17)

Since generally $\beta < 0$, this requires that salt needs to be removed at greater depth and added at shallower depth. Large vertical variations in $g\alpha$ and $g\beta$ can be accounted for using the generalized relation in Equations (14) and (15), which allow us to compute the mechanical energy input associated with any given heat and salt flux boundary conditions more generally. When horizontal variations in the thermal and haline expansion coefficient are nonnegligible, the amount of energy that can be converted to kinetic energy depends on the specifics of the circulation, as elaborated on in the Appendix.

Equations (14) and (15) also highlight the potential role of vertical diffusion. Indeed, buoyancy gain and loss at the same level combined with vertical diffusion can drive circulation, which is sometimes referred to as horizontal convection (e.g., Sandström 1908; Paparella & Young 2002; Wunsch & Ferrari 2004; Hughes & Griffiths 2008). As the energy source in such a circulation is derived from diffusion, the energy dissipation has to go to zero in the limit of vanishing diffusivity. As a result, Paparella & Young (2002) argue that no "turbulent" circulation can be maintained in the limit of vanishing diffusivity (and viscosity), where "turbulence" is defined to imply a forward energy cascade with a dissipation rate that becomes independent of the viscosity.[8] In reality, molecular diffusion is not vanishingly small, and we will discuss its potential role below. It is also worth noting at this point that many numerical simulations employ strongly enhanced "eddy diffusivities," which can act as a substantial energy source in numerical simulations. However, it is important to remember that these parameterizations are meant to represent the effect of turbulent advection—that is, they parameterize the unresolved contribution to the wb term in Equation (3). The apparent energy source associated with parameterized "eddy diffusion" therefore needs to be interpreted as a conversion of unresolved turbulent kinetic energy to potential energy, and accordingly can be justified only if there exists a corresponding source of unresolved turbulent kinetic energy.

2.2. Energy Dissipation and Flow Properties

In equilibrium, the total sources and sinks of mechanical energy have to be in balance. The energy sources thereby provide a constraint on the energy dissipation, which in turn provides some constraint on the flow. Relating the energy dissipation rate to the kinetic energy of the flow itself is not straightforward, as it depends on the characteristics of the flow field, but we can make some progress by considering specific flow regimes and estimating the range of parameters and scales over which the flow regimes are expected to hold. In the following, we first discuss the relationship between the kinetic energy and the dissipation rate for a turbulent flow that is largely unaffected by rotation, as well as the conditions under which the assumption that rotation is negligible breaks down. We then derive an alternative relationship between the kinetic energy and the dissipation rate in the opposite limit where rotation is a leading-order effect and the most energetic flows

---

[8] Notice that, unlike 3D turbulence, 2D (and geostrophic) "turbulence" does not generally exhibit a forward energy cascade, making it not truly "turbulent" by this definition. We will address constraints for geostrophic turbulence in Section 2.2.1.

are geostrophically balanced (i.e., the leading-order momentum balance is between the pressure gradient and Coriolis acceleration).

2.2.1. Isotropic Turbulence and the Role of Rotation

We first assume a fully turbulent flow unconstrained by the influence of rotation in the interior (i.e., away from the boundaries), and we assume that, in this limit, the dissipation rate is independent of the value of molecular viscosity. In particular, we start by considering Kolmogorov's theory for the kinetic energy spectrum in the inertial cascade of isotropic turbulence, which suggests that

$$E(k) = \mathcal{K}\epsilon^{2/3}k^{-5/3}, \tag{18}$$

where $E(k)$ is the kinetic energy spectrum as a function of the wavenumber, k, ϵ is the turbulent spectral KE flux, which in turn is equal to the dissipation rate, and $\mathcal{K} \approx 1.5$ is the Kolmogorov constant (e.g., Vallis 2006). Integrating over the energy inertial range yields

$$E_t \approx 2k_0^{-2/3}\epsilon^{2/3}, \tag{19}$$

where k_0 is the "injection scale" (where the KE spectrum flattens out), and E_t is the total turbulent kinetic energy in the inertial range.

We can use Equation (19) to estimate the kinetic energy of turbulent flows up to the largest scales of an isotropic turbulent energy inertial range. Isotropy may be broken by the geometry (e.g., the vicinity to a boundary), or by the effects of stratification or rotation. We will here consider in particular the importance of rotation, which can break isotropy and fundamentally change the nature of the turbulent flow throughout the water column.

The effect of rotation on the turbulent flow in the interior can be characterized by the flow Rossby number, which we here define as the ratio of the inverse "eddy turnover timescale," $\tau_{\text{eddy}}^{-1} \sim \sqrt{E_t}k_0$, to the rotation rate, Ω. This ratio measures the relative magnitude of the nonlinear advection term to the Coriolis term in the momentum equation, and thus provides a useful and widely used measure for the role of rotation in the dynamics of high-Reynolds-number flows (e.g., Vallis 2006). Using Equation (19), and $L \equiv 2\pi/k_0$, the turbulent flow Rossby number can be estimated as

$$\text{Ro}_t \equiv \frac{\sqrt{E_t}}{\Omega L} \approx \frac{\epsilon^{1/3}}{\Omega L^{2/3}}. \tag{20}$$

Equation (20) suggests a maximum length scale for turbulent flows unaffected by rotation (see also Fernando et al. 1991; Jones & Marshall 1993; Maxworthy & Narimousa 1994; Bire et al. 2022):

$$L_{\text{rot}} \approx \frac{\epsilon^{1/2}}{\Omega^{3/2}}. \tag{21}$$

Maxworthy & Narimousa (1994) and others found that, once rotation becomes important, the convective Rossby number of a rotating plume in the interior scales as

$$\text{Ro}_{\text{rc}} = \frac{\epsilon^{1/2}}{\Omega^{3/2}H}, \tag{22}$$

where H is the depth of the convecting fluid. Equation (22) is likely to be a better predictor of the convective flow Rossby

number when ocean depth convection is strongly affected by rotation (i.e., $L_{\text{rot}} < H$). If we set $L = H$, we find $\text{Ro}_{\text{rc}} = \text{Ro}_t^{3/2}$, and hence both definitions give the same prediction for the critical length/depth scale at which $Ro \approx 1$ and rotation becomes important,[9] which indeed also follows directly from dimensional analysis if we postulate that this scale shall depend only on ϵ and Ω. If this length scale is significantly smaller than the scale of the most energetic flows, we expect these flows to be strongly affected by rotation. For convective flows unconstrained by rotation, the natural length scale for the largest convective motion is the depth of the ocean, such that we expect the interior convective dynamics to become strongly affected by rotation if L_{rot} is much smaller than the depth of the ocean (see also Fernando et al. 1991).

2.2.2. Boundary-layer Dissipation in Geostrophic Dynamics

When rotation becomes of dominant importance it is likely that much of the energy becomes trapped in geostrophically balanced vortices and large-scale mean flows, which result from the upscale kinetic energy cascade associated with quasi-balanced turbulent motions (e.g., Vallis 2006). The lack of a forward energy cascade means that dissipation is likely to be limited mostly to turbulent boundary layers near the seafloor and the ice–ocean interface.

We can estimate the energy dissipation per unit area in a turbulent boundary layer as (e.g., Jansen 2016, and references therein):

$$\int \epsilon_{\text{BL}}dz = c_D|U_g|^3, \tag{23}$$

where the integral on the lhs is over the depth of the turbulent boundary layer, c_D is the turbulent drag coefficient, and U_g is the characteristic near-surface geostrophic velocity. The value of c_D depends on the surface roughness, with $c_D \approx 0.0025$ an empirical average value that is commonly used for the drag coefficient for Earth's seafloor (e.g., Egbert et al. 2004; Sen et al. 2008). The skin drag coefficient under smooth ice can be estimated to be around $c_D \approx 0.002$, although rough morphology can significantly increase this value (e.g., Brenner et al. 2021). Lacking information about the ice roughness, and noting the order-of-magnitude nature of our estimates, we will here use $c_D \approx 0.001$–0.01 at both the seafloor and under the ice sheet at the top. Experience from oceanic and atmospheric modeling has shown that drag coefficients of this order produce reasonable results for a wide range of flows (e.g., Smagorinsky et al. 1965; Egbert et al. 2004; Sen et al. 2008; Chen et al. 2018; Adcroft et al. 2019), which instills confidence that a similar coefficient can be used to obtain useful order-of-magnitude estimates for icy-moon oceans.

---

[9] Aubert et al. (2001) defines the parameter $\gamma = \alpha g Q_{\text{bot}}/(\rho c_p \Omega^3 H^2) = \epsilon/(\Omega^3 H^2)$ to characterize rotating convection at high Reynolds numbers, where in the second equality we assumed a balance between potential energy generation by the heat flux forcing and kinetic energy dissipation. With this parameter, we can write $Ro_t \sim \gamma^{1/3}$ while $Ro_{\text{rc}} \sim \gamma^{1/2}$. Aubert et al. (2001) and others (e.g., Cardin & Olson 1994; Gastine et al. 2016) suggested that $Ro \sim \gamma^{2/5}$ in the highly nonlinear limit of rapidly rotating convection, thus giving an intermediate power dependence of Ro on γ. However, all scaling relations give the same result for the threshold where $Ro \sim 1$.

Averaging the energy dissipation in the top and bottom boundary layers over the depth of the whole water column gives an average energy dissipation rate per unit volume

$$\epsilon_{\rm BL} \approx \frac{2^{5/2}c_D}{H}E_g^{3/2}, \qquad (24)$$

where H is the depth of the ocean, and $E_g = 1/2|U_g|^2$ is the characteristic KE of the geostrophic flow. We can solve Equation (24) to get a crude estimate for the characteristic KE in a flow that is dominated by large-scale balanced dynamics, where KE dissipation occurs primarily in turbulent boundary layers:

$$E_g \approx \frac{H^{2/3}}{2^{5/3}c_D^{2/3}}\epsilon_{\rm BL}^{2/3}. \qquad (25)$$

In general, balanced dynamics may coexist with intermediate-Rossby-number and high-Rossby-number convective turbulence and/or tidal waves, in which case interior energy dissipation may be important and thus $\epsilon_{\rm BL} = \epsilon - \epsilon_{\rm int} < \epsilon$, where $\epsilon_{\rm int}$ denotes energy dissipation away from the boundary layers. It is also important to note that numerical simulations of planetary circulation typically use very high artificial viscosities for numerical stability, which can lead to a large, albeit probably unphysical, dissipation of balanced KE in the interior (e.g., Jansen 2016).

3. Scaling Laws for the Kinetic Energy of Thermally Driven Flows on Snowball Earth, Enceladus, and Europa

We can derive estimates for the kinetic energy of buoyancy-driven flows by assuming a statistically steady state where the source of KE equals the sink. If the primary source of mechanical energy is given by thermal buoyancy forcing, Equation (4) together with Equations (11) and (14) provide a scaling relation for the mean kinetic energy dissipation per unit volume:

$$\epsilon \equiv \frac{1}{V}\int \boldsymbol{v}\cdot\mathcal{D} \sim \frac{\mathcal{B}^\theta}{V} \approx \frac{g\alpha\mathcal{F}^Q H}{\rho c_p V} \approx \frac{Q\alpha g}{\rho c_p}, \qquad (26)$$

where Q is the average heat flux through the seafloor per unit area, and for now we neglect variations in the thermal expansion coefficient, α, as well as radial variations in the gravity and the surface area throughout the depth of the ocean. (The latter assumption leads to O(10%) errors for Europa and Enceladus, which is not of concern here. The former may lead to larger errors if the ocean is relatively fresh, and we will return to this issue later.) We also ignored the energetic effect of molecular diffusion (the second term in Equation (14)), which is likely to be small if the ocean is convective.[10] We will return to the potential importance of molecular diffusion in a stratified ocean below.

Equation (26) provides a key constraint for the energetics of thermally driven flows. It predicts that the energy dissipation rate per unit volume increases linearly with the bottom buoyancy flux, which in turn is given by the heat flux multiplied by the thermal expansivity and the gravity. The results are shown in Figure 3 for the parameter range occupied by the icy moons and Snowball Earth. In the following, we use
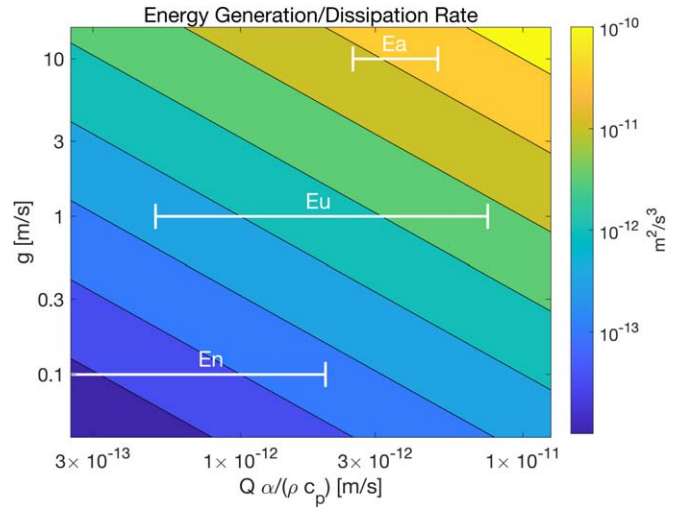
---

[10] Notice that this formally amounts to assuming a large Nusselt number—i.e., we assume that the advective heat flux is large compared to the diffusive heat flux.

Figure 3. Energy dissipation rate per unit volume for thermally driven flows predicted by the scaling in Equation (26) as a function of the bottom heat flux (Q) times $\alpha/(\rho c_p)$ and the gravitational acceleration (g). The white bars mark the estimates for Snowball Earth (Ea), Europa (Eu), and Enceladus (En), assuming the parameters given in Table 1. The color bar is logarithmic with contours at $10^{-13.5}, 10^{-13}, ..., 10^{-10.5}$ m^2 s^{-3}.

this result together with the results from Sections 2.1 and 2.2 to obtain order-of-magnitude estimates for thermally driven ocean flows on Snowball Earth, Europa, and Enceladus.

To estimate the kinetic energy dissipation rate for thermally driven flows in the oceans of Snowball Earth, Europa, and Enceladus, we assume an average heating rate at the ocean floor of $Q \approx 0.1$ W m^{-2} for Snowball Earth (Korenaga 2008), $Q \approx 0.02$–0.1 W m^{-2} for Europa (Ruiz 2005; Vance et al. 2018), and $Q \approx 0.01$–0.08 W m^{-2} for Enceladus (Čadek et al. 2016; Choblet et al. 2017; Hemingway et al. 2018; Vance et al. 2018). The gravitational acceleration is $g \approx 10$ m s^{-2} for Earth, $g \approx 1$ m s^{-2} for Europa, and $g \approx 0.1$ m s^{-2} for Enceladus. The thermal expansion coefficient depends on the temperature, salinity, and pressure. The salinity in the Snowball Earth ocean was likely between around 40–70 g kg^{-1} (e.g., Ashkenazy et al. 2013) while the pressure would have ranged from $\sim$100 bar under the ice sheet to $\sim$400 bar at the seafloor. Assuming temperatures near the freezing point, this suggests a mean ocean thermal expansivity of around $\alpha \approx 1-2 \times 10^{-4}$ K^{-1}. Salt concentration (and composition) on Europa is poorly constrained and may be anywhere below about 100 g kg^{-1} (Vance et al. 2018). The pressure may be as low as 50 bar below a 5 km deep ice shell and reach $\gtrsim$1000 bar at the seafloor. Assuming temperatures near the freezing point, the mean ocean thermal expansivity is expected to be $\alpha \approx 1-3 \times 10^{-4}$ K^{-1} (although α may be vanishingly small at the bottom of the ice shell). The salinity on Enceladus has been estimated to be around 5–30 g kg^{-1} (Glein et al. 2018). Due to the relatively low pressures on Enceladus ($\lesssim$50 bar), the thermal expansion coefficient near the freezing point would be negative if the salinity is $\lesssim$20 g kg^{-1} (Zeng & Jansen 2021; Kang et al. 2022), and we will return to this low-salinity scenario in Section 3.3. In general, we expect $\alpha < 10^{-4}$ K^{-1} for Enceladus. All parameters and assumed uncertainties are summarized in Table 1. Using further that $\rho c_p \approx 4 \times 10^6$ J m^{-3} K^{-1} on all bodies, we find

$$\epsilon \approx 2.5\text{–}5 \times 10^{-11} \text{ m}^2\text{ s}^{-3} \quad \text{for Snowball Earth,} \qquad (27)$$

$$\epsilon \approx 5 \times 10^{-13}\text{–}8 \times 10^{-12} \text{ m}^2\text{ s}^{-3} \quad \text{for Europa,} \qquad (28)$$
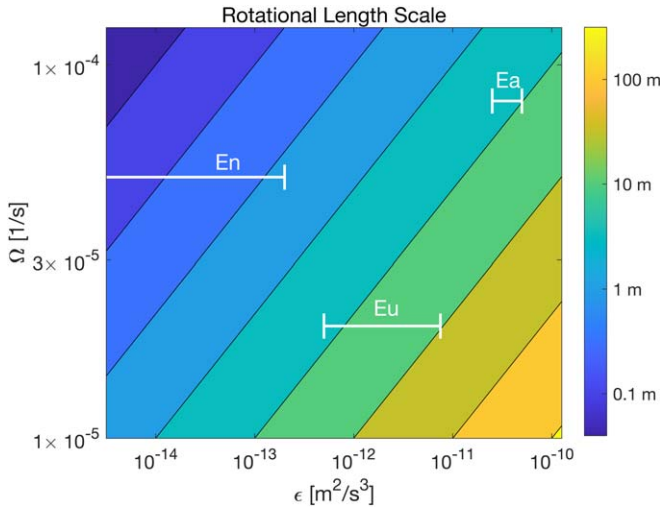
Figure 4. Estimated length scale above which turbulence in the interior is expected to become strongly affected by rotation, as predicted by the scaling in Equation (21), as a function of the turbulent dissipation rate (ϵ) and the rotation rate (Ω). The white bars mark the estimates for thermally driven circulation in Snowball Earth (Ea), Europa (Eu), and Enceladus (En), assuming the parameter ranges given in Table 1. The markers indicating Snowball Earth, Europa, and Enceladus further assume that most of the turbulent kinetic energy dissipation occurs in the interior. If the dissipation is dominated by boundary layers, the markers would move to the left, thus further reducing the length scale where the interior flow would become strongly affected by rotation. The color bar is logarithmic with contours at 10^{-1} m, $10^{-0.5}$ m, ..., $10^{2.5}$ m.

$$\epsilon \lesssim 2 \times 10^{-13} \, \text{m}^2 \, \text{s}^{-3} \quad \text{for Enceladus.} \qquad (29)$$

The energy dissipation rate is thus likely to be the largest for Snowball Earth and the smallest for Enceladus, with the differences mostly driven by the differences in the gravity and further amplified by differences in the estimated vertical heat flux and thermal expansivity. For comparison, the kinetic energy dissipation rate in Earth's deep ocean today is around 2 TW (Wunsch & Ferrari 2004), which divided by the mass of the ocean amounts to about $1.5 \times 10^{-9} \, \text{m}^2 \, \text{s}^{-3}$. This dissipation is balanced by the energy input primarily from winds and tides, which provide significantly more energy to the present-day ocean circulation than geothermal heating.

3.1. The Role of Rotation

Given the energy dissipation rate, ϵ, and the rotation rate of the planetary body, Ω, we can use Equation (21) to estimate a critical scale L_{rot} above which we may expect turbulent motions to become strongly affected by rotation (Figure 4). Using the energy dissipation rates estimated above and $\Omega \approx 8 \times 10^{-5} \, \text{s}^{-1}$ for Snowball Earth, 5×10^{-5} s^{-1} for Enceladus, and 2×10^{-5} s^{-1} for Europa, we find the scale at which convection is expected to become strongly affected by rotation from Equation (21) to be $L_{\text{rot}} \sim O(10 \, \text{m})$ for Snowball Earth and Europa and $L_{\text{rot}} \lesssim 1$ m for Enceladus. In addition to parametric uncertainties (quantified in Figure 4 and Table 2), it is possible that assumptions leading to Equation (21) may not hold. In particular, we here assumed that the interior dissipation (which enters the scaling for L_{rot}) is of similar order as the total kinetic energy dissipation. If the dissipation is dominated by boundary layers, the length scale where the interior flow would become strongly affected by rotation would be further reduced. Regardless, L_{rot} is much smaller than the ocean depth in all three cases, and we therefore expect deep convection and any

other potential large-scale flow to be strongly affected by rotation. It is also worth noting that, for Snowball Earth and Europa, L_{rot} is likely to be much larger than the Kolmogorov scale where viscous dissipation occurs, $L_\nu = (\nu^3/\epsilon)^{1/4}$, which is expected to be on the order of a few centimeters, thus indicating that an isotropic inertial range is expected to exist at scales smaller than L_{rot}. On Enceladus it is not clear whether L_{rot} is significantly larger than the Kolmogorov scale, raising the possibility that no isotropic cascade exists. In that case, the relationship in Equation (18) may not be expected to hold at any scale, but the conclusion that the large-scale flow would be strongly affect by rotation would remain true, as indeed the flow at all scales (down to the viscous dissipation scale) would be strongly affected by rotation. We also note that, for all icy oceans considered here, L_{rot} is significantly smaller than the smallest length scales that can be resolved in global-scale numerical simulations of these oceans, suggesting that large-eddy-simulations that can explicitly resolve part of the isotropic turbulent inertial range are not feasible with realistic parameters (see Bire et al. 2022).

3.1.1. Comparison to Existing Simulation Results

The importance of rotation in the oceans of Snowball Earth, Europa, and Enceladus is qualitatively consistent with the Snowball Earth simulations of Ashkenazy et al. (2013) and Jansen (2016), the Europa simulations of Ashkenazy & Tziperman (2021), and the Enceladus simulations of Kang et al. (2020, 2022) and Zeng & Jansen (2021). For illustration, Figures 5 and 6 show simulation results from Jansen (2016) and Zeng & Jansen (2021) for heating-driven flows in the oceans of Snowball Earth and Enceladus, respectively.

The flow field in the Snowball Earth simulation shows a horizontal eddy field characteristic of geostrophic turbulence (Figure 5(b)), with the flow largely barotropized—i.e., varying little in the vertical (Figure 5(b)). The characteristic vertical-flow Rossby numbers are small (Figure 5(a)), qualitatively consistent with the predictions in Section 2.2.1. However, we notice that the vertical flows here are associated with the quasi-geostrophic eddies rather than convection, as geostrophic eddies establish a statically stable stratification. Neither of the convective Rossby-number scalings in Equations (20) and (22) are therefore expected to apply to this flow (although the conclusion that rotation is important still holds, as it is indeed a necessary condition for the development of quasi-geostrophic eddies in the first place).

The vertical-flow Rossby numbers in the high-salinity Enceladus ocean simulations of Zeng & Jansen (2021) are even smaller and show a pattern of grid-scale convection (Figure 6(a)). The grid-scale convection is qualitatively consistent with the prediction that the scale at which rotation affects convective plumes (O(1m)) is much smaller than the model resolution (~1 km), but unfortunately also implies that the details of the simulated flow are expected to be sensitive to the model resolution and somewhat arbitrary modeling choices, such as parameterized "eddy" viscosities and diffusivities (see Zeng & Jansen 2021). Nevertheless, the importance of rotation is robust and can also be seen in the organization of the zonal mean flow into jets that are approximately aligned with the axes of rotation (Figure 6(c)).

The result that flows are very strongly affected by rotation may appear at odds with simulation results for Europa's ocean by Soderlund et al. (2014), which show strong turbulent
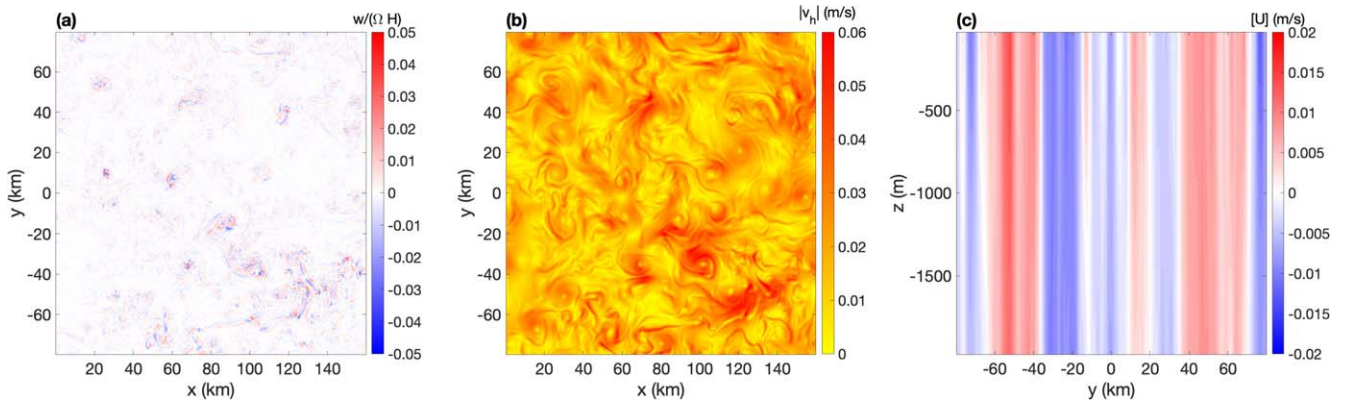
Figure 5. Results from an idealized Snowball Earth ocean simulation, originally presented in Jansen (2016). (a) Snapshot of the nondimensional vertical velocity normalized as $w/(\Omega H)$, where Ω is the planetary rotation rate and H is the ocean depth, such as to provide a flow Rossby number. (b) Snapshot of the horizontal flow speed near the seafloor. (c) Snapshot of the zonal mean zonal flow (as a function of the depth and latitude). The model simulates a buoyancy-driven flow associated with a spatially inhomogeneous bottom heating with a mean of 0.1 W m^{-2}, crudely mimicking the expected dynamics in a Snowball Earth ocean. The simulation uses a linear equation of state with thermal expansivity $\alpha = 1 \times 10^{-4}$ K^{-1} and an idealized Cartesian-coordinate domain representative of the mid latitudes (see Jansen 2016 for additional details).

convection with relatively moderate flow Rossby numbers. The apparent contradiction can readily be understood by noting that the dimensional vertical heat flux in the DNS of Soderlund et al. (2014) would amount to about 10^5 Wm^{-2} after redimensionalizing with Europa's planetary parameters—versus a heat flux of 0.02–0.1 Wm^{-2} assumed here. Increasing the vertical heat flux on Europa to 10^5 Wm^{-2} would yield $L_{\rm rot} \approx 25$ km, which in turn would make significant turbulent convection that is only relatively weakly affected by rotation plausible. Indeed, using Equation (20) with $L \approx H \approx 100$ km (for the depth of Europa's ocean) and a heat flux of 10^5 Wm^{-2} (which gives $\epsilon \approx 5 \times 10^{-6}$ m^2 s^{-3}) we can estimate a Rossby number for full-depth turbulent convection of Ro$_t \approx 0.4$, which is broadly consistent with the Rossby numbers of convective motions found in the simulations of Soderlund et al. (2014). The large implied dimensional heat flux in the DNS of Soderlund et al. (2014) is meant to account for the large viscosities and diffusivities that are necessary in numerical simulations. However, the energetic argument discussed here clarifies that the greatly amplified heat flux is expected to lead to much larger dimensional flow speeds. Hence, the magnitude of the dimensionalized velocities from the DNS of Soderlund et al. (2014), and the associated large-scale-flow Rossby numbers, should not be taken at face value.

In summary, our results suggest that the turbulent flow characteristics in the ocean's interior are strongly constrained by the rate of energy input, which in the case of thermally driven flows is given by the vertical heat flux, and the nature of the energy dissipation. The dissipation mechanisms and in some cases the energy source are likely to be misrepresented in numerical modeling studies, which cannot resolve all relevant scales of motion. The quantitative results of icy-moon ocean simulations therefore need to be interpreted with care.

3.2. Quasi-balanced Flows

At scales much larger than $L_{\rm rot}$, we expect the motion to be strongly affected by rotation, leading to quasi-balanced flows that do not undergo a forward energy cascade. Energy dissipation then may be limited mostly to turbulent boundary layers, such that we can assume $\epsilon_{\rm BL} \sim \epsilon$. In this case,

Equation (25) may provide a useful estimate for the total KE and thus typical flow speeds as a function of the energy dissipation rate, ϵ, and the depth of the ocean, H (Figure 7). Assuming an ocean depth of $H \approx 2 - 3$ km for Snowball Earth (Ashkenazy et al. 2013; Yang et al. 2017), $H \approx 50 - 150$ km for Europa (Anderson et al. 1998; Vance et al. 2018), and $H \approx 10$–50 km for Enceladus (Čadek et al. 2016; Hemingway et al. 2018; Vance et al. 2018), we find

$$E_g \approx 10^{-4}\text{–}10^{-3} \text{ m}^2 \text{ s}^{-2} \quad \text{for Snowball Earth}, \tag{30}$$

$$E_g \approx 5 \times 10^{-5}\text{–}3 \times 10^{-3} \text{ m}^2 \text{ s}^{-2} \quad \text{for Europa}, \tag{31}$$

$$E_g \lesssim 10^{-4} \text{ m}^2 \text{ s}^{-2} \quad \text{for Enceladus}. \tag{32}$$

These results suggest potential balanced flow velocities of up to a few cm s^{-1} for Snowball Earth and Europa and up to one cm s^{-1} for Enceladus. These estimates should generally be viewed as upper bounds as we here assumed that all energy input goes into balanced motions that are dissipated only in the boundary layers, while we ignored any potential additional dissipation in the interior, which would reduce the expected kinetic energy level.

3.2.1. Comparison to Existing Simulation Results

Flow velocities on the order of centimeters per second are broadly consistent with the Snowball Earth simulations of Jansen (2016; Figure 5(b)), as well as the Snowball Earth simulations of Ashkenazy et al. (2013) and Europa simulations of Ashkenazy & Tziperman (2021). Figure (8)) shows the energy budget terms for the Snowball Earth simulation of Jansen (2016; see Figure 5(b) for the corresponding flow fields). As assumed in our scaling argument, the primary energy source is associated with the vertical heat flux imposed by the seafloor heating, whose magnitude $\mathcal{B}_{\mathcal{F}}^{\Theta}/V \sim \epsilon \approx 2.5 \times 10^{-11}$ m^2 s^{-3} is consistent with our estimate in Equation (28). Somewhat more than half of this kinetic energy is dissipated at the boundary (where the model uses a quadratic drag, consistent with the assumption in Equation (23)), with the remainder dissipated by viscous dissipation in the interior. It is likely that the interior dissipation is unrealistically large in the
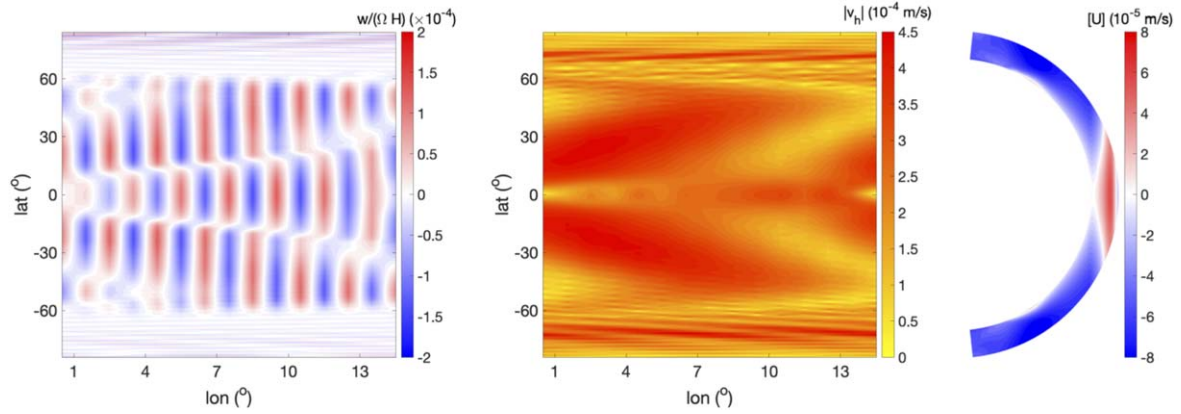
Figure 6. Results from an idealized high-salinity Enceladus ocean simulation, originally presented in Zeng & Jansen (2021). (a) Snapshot of the nondimensional vertical velocity normalized as $w/(\Omega H)$, where is the planetary rotation rate and H is the ocean depth, such as to provide a flow Rossby number. (b) Snapshot of the horizontal flow speed near the seafloor. (c) Snapshot of the zonal mean zonal flow (as a function of the depth and latitude). The model simulates a buoyancy-driven flow associated with a spatially inhomogeneous bottom heating with a mean of 0.04 W m^{-2}, crudely mimicking the conditions in Enceladus' ocean. The simulation assumes a spatially constant salinity of 35 g kg^{-1} with an Earth-like salt composition and simulates the flow in a 15° wide sector of a spherical shell (see Zeng & Jansen 2021 for additional details).
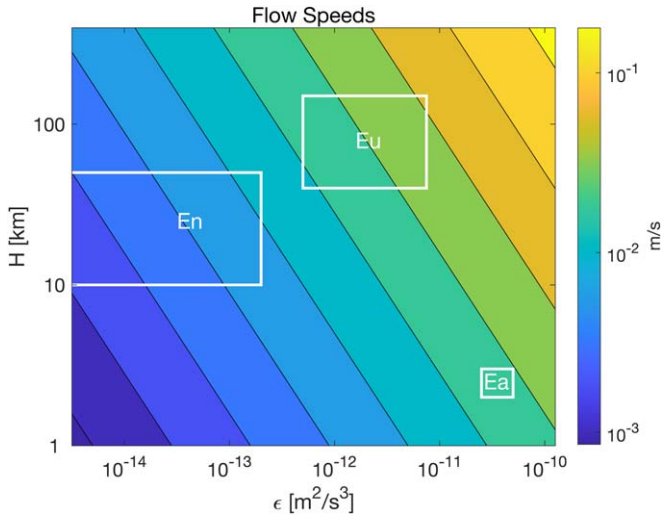

Figure 7. Estimated geostrophic flow speeds ($U_g = \sqrt{2E_g}$) as a function of the energy dissipation rate (ϵ) and ocean depth (H) as predicted by the scaling in Equation (25) assuming that most dissipation happens in turbulent boundary layers near the seafloor and ice–ocean interface with a drag coefficient of $C_d = 0.025$. Notice that a 1 order of magnitude uncertainty in C_d would amount to an uncertainty in the flow speed of just over a factor of 2 ($10^{1/3}$). The white boxes mark the estimated locations for Snowball Earth (Ea), Europa (Eu), and Enceladus (En), assuming the parameter ranges given in Table 1. The color bar is logarithmic with contours at 10^{-3} m s^{-1}, $10^{-2.75}$ m s^{-1}, ... , $10^{-0.75}$ m s^{-1}.

simulations due to the limited resolution and required large "eddy" viscosity. However, the interior dissipation does not affect the order of magnitude of the velocity as long as boundary friction is a first-order contributor to dissipation, and hence the simulated velocities are consistent with the prediction in Equation (30).

The high-salinity Enceladus ocean simulation of Zeng & Jansen (2021) has flow velocities on the order of 10^{-4} m s^{-1} (Figure 6), which is broadly similar to results reported in Kang et al. (2020) but 2 orders of magnitude weaker than our estimate for the maximum flow speeds (Equation (32)). The parameters used in the Enceladus simulation of Zeng & Jansen (2021) are expected to place the energy input about a factor of 10 below our upper bound estimate, which by itself would translate to flow speeds that are only about a factor of 2 below

the predicted maximum (see Equation (23)). Some discrepancies may be expected due to the parameterized boundary-layer drag. Instead of the quadratic boundary-layer drag assumed in Equation (24), the simulations of Zeng & Jansen (2021; and also Kang et al. 2020) apply a relatively strong linear drag parameterization. However, the stronger boundary-layer drag (which can readily be incorporated into the scaling law) can only explain a relatively small part of the misfit. Instead, interior viscous dissipation is key to explaining the much weaker velocities in the simulations, as shown explicitly in Figure 8(b) for the Enceladus simulation of Zeng & Jansen (2021). Strong dissipation of kinetic energy associated with the (numerically necessary) large interior viscosity implies that the total dissipation rate is much larger than the boundary-layer dissipation (i.e., $\epsilon \gg \epsilon_{BL}$), thus leading to much weaker velocities. The large viscosities in the simulations (which cannot resolve the inertial cascade range) cannot be justified on physical grounds. Whether a dominant contribution from interior dissipation is likely to exist on Enceladus, or is purely an artifact of insufficient resolution and artificially large viscosity in the simulations, remains unknown and depends on how efficiently energy is transferred into balanced motions. In either case, the estimate in Equation (32) is expected to remain valid as an upper bound, although the true velocities may be much smaller.

The Europa simulations of Soderlund et al. (2014) as well as the Enceladus-like small Ekman number simulations of Soderlund (2019) suggest much larger velocities than estimated here (if redimensionalized with the actual ocean depth and rotation rate of the respective icy moons). Qualitatively, this discrepancy may be expected as a result of the much larger dimensional vertical heat flux, which leads to a much larger energy source, as discussed above. However, the scaling argument leading to Equation (25) is not expected to apply to the simulations of Soderlund et al. (2014) and Soderlund (2019), due to different boundary conditions, thus not allowing for a quantitative prediction of their simulation results. In particular, Soderlund et al. (2014) and Soderlund (2019) use smooth boundaries with free-slip boundary conditions, which implies no boundary drag.
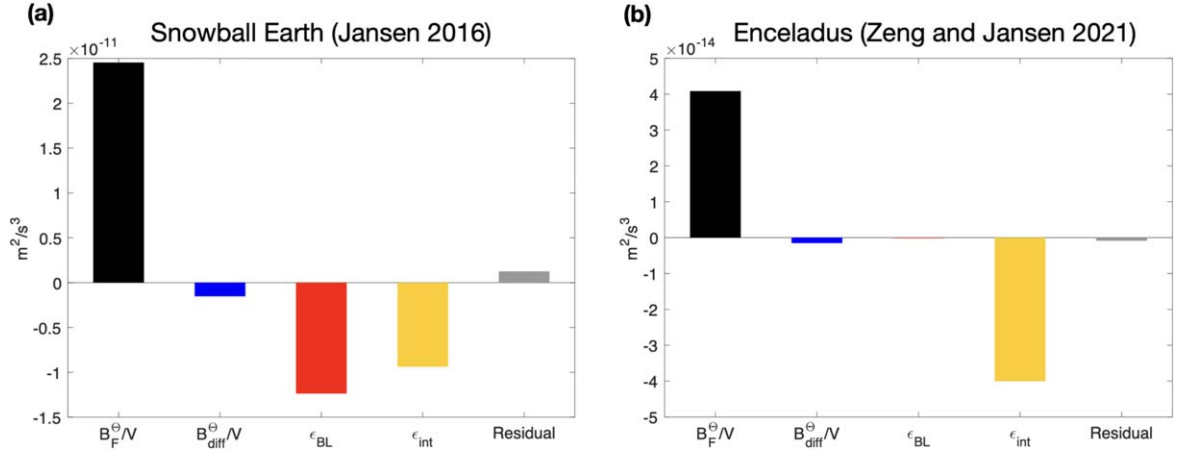
Figure 8. Mechanical energy budget of (a) the Snowball Earth ocean simulation from Jansen (2016) and (b) the Enceladus ocean simulation from Zeng & Jansen (2021). From left to right are the energy sources and sinks (per unit volume) due to heat flux forcing at the boundaries ($\mathcal{B}_{\mathcal{F}}^{\Theta}/V$), vertical diffusion ($\mathcal{B}_{\text{diff}}^{\Theta}/V$), parameterized boundary-layer dissipation (ϵ_{BL}), and interior viscous dissipation (ϵ_{int}). The last bar shows the residual associated with nonequilibrium effects and errors in our offline calculation of the energy budgets.
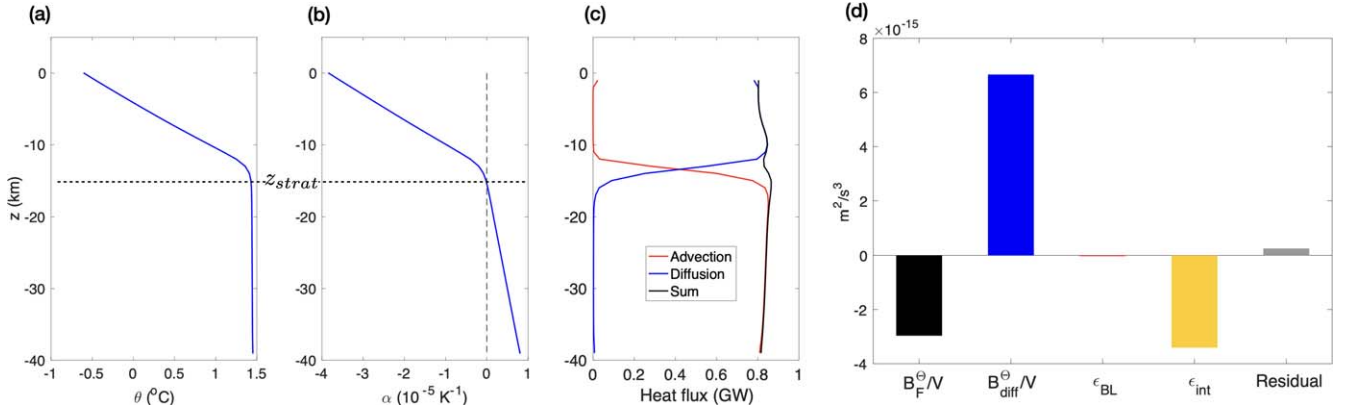

Figure 9. Results from the Enceladus ocean simulation with low salinity from Zeng & Jansen (2021; as described in Figure 6 but with salinity 8.5 g kg^{-1}). Although the ocean is heated from below, convection is suppressed in the upper ocean as the thermal expansivity is negative near the freezing point. (a) Temperature; (b) thermal expansivity; (c) advective (red), diffusive (blue), and total (black) vertical heat flux, all as a function of the depth. Panel (d) shows the energy budget decomposition as in Figure 8. Panels (a)–(c) are reproduced from Zeng & Jansen (2021).

3.3. Thermally Driven Flows in a Low-salinity, Low-pressure Ocean

If salinity and pressure are relatively low, the thermal expansion coefficient near the freezing point is negative. This scenario was first suggested for Europa by Melosh et al. (2004), although due to the modest pressures that are required for a negative thermal expansion coefficient, it appears most likely to be relevant for Enceladus, and was considered in the low-salinity Enceladus ocean simulations of Zeng & Jansen (2021) and Kang et al. (2022). To estimate the energetics of such an ocean, we assume a stably stratified layer below the ice sheet and above some depth z_{strat}, as found in the low-salinity simulation of Zeng & Jansen (2021; Figure 9). In the stratified layer, the temperature decreases upward from the "critical temperature," Θ_c, where $\alpha(\Theta_c, z_{\text{strat}}) = 0$ to the freezing point, Θ_f, at the bottom of the ice sheet, z_{ice} (where $\alpha(\Theta_f, z_{\text{ice}}) < 0$). For illustrative purposes, we assume that the seafloor and ice sheet are flat (i.e., both boundaries follow a geopotential height surface), such that $\mathcal{F}^{\mathcal{Q}}$ is vertically constant and equal to the total bottom heat flux. Assuming again that horizontal variations in the thermal expansion coefficient are small,

Equation (14) gives the KE generation as

$$\mathcal{B}^{\Theta} = \int g \langle \alpha \rangle \left[\frac{\mathcal{F}^{\mathcal{Q}}}{\rho c_p} + A\kappa_T \partial_z \langle \theta \rangle \right] dz. \tag{33}$$

In the stratified layer, $\langle \alpha \rangle < 0$, such that the first term in the integral in Equation (33) amounts to an energy sink. One plausible solution is then that the vertical heat flux through the stratified layer is balanced by molecular diffusion (i.e., the second term in the integral in Equation (33)), which amounts to a conversion from internal to potential energy. In this case the stratified layer would only be a few tens of meters thick (Zeng & Jansen 2021), and most of the ocean would be convective with $\Theta > \Theta_c$ and hence $\alpha > 0$. The dynamics in the convective layer would follow scaling laws analogous to those presented above, although the very small thermal expansion coefficient at temperatures only marginally warmer than Θ_c implies that the energy input and hence maximum flow speeds would be much smaller than the upper bound estimated above.

The simulations of Zeng & Jansen (2021) used a relatively large "eddy diffusivity" ($\kappa_z = 5 \times 10^{-5}$ m^2 s^{-1}), chosen such as

to obtain a well-resolved stratified layer with negative thermal expansivity, above a convective deep ocean with weakly positive thermal expansivity (Figure 9(a),(b)). The vertical heat flux through the stratified layer is balanced by this "eddy diffusion" (Figure 9(c)), such that from the perspective of the model's energetics, the two terms in the integral in Equation (33) balance in the stratified layer. Below the stratified layer, the thermal expansivity is positive such that convective upward heat flux releases kinetic energy that can balance dissipation. Integrated over the entire ocean, however, diffusion is the only net energy source and balances the energy loss associated with net upward heat flux and the viscous dissipation (Figure 9(d)). The simulations of Kang et al. (2022) used an even larger eddy diffusivity ($\kappa = 5 \times 10^{-3}$ m^2 s^{-1}), such that the entire depth of the ocean becomes stratified with the upward heat flux and associated downward buoyancy flux accomplished by "eddy diffusion" (not shown). However, in both studies the model's diffusivities, which are much larger than the molecular value, need to be interpreted as representing turbulent mixing. If these turbulent mixing rates are real, the associated vertical heat flux represents turbulent advection, which amounts to a negative $\mathcal{B}^\Theta$ - that is a conversion of turbulent kinetic energy to large-scale potential energy. An additional implied energy source is therefore needed to generate the turbulent kinetic energy and justify the applied eddy diffusivities. A possible source are tides and/or librations, to which we will return below.

4. Salinity Forcing

A number of studies have recently argued for the importance of salt forcing in driving a circulation on Europa and Enceladus (Zhu et al. 2017; Kang et al. 2020; Ashkenazy & Tziperman 2021; Lobo et al. 2021; Kang et al. 2022). Because β, as defined in Equation (10), is always negative, salinity forcing provides a source of mechanical energy if, and only if, salt is added (e.g., by freezing) at a shallower depth and removed (or fresh water is added by melting) at a greater depth (Equations (13) and (15)). At steady state, however, freezing and melting need to balance the convergence of ice flow, which tends to flow from regions of thick ice to regions of thin ice. We therefore expect melting to occur where the ice is thin, and hence the ice–ocean interface is shallow, while freezing occurs where the ice is thick and hence the ice–ocean interface is deep (see Figure 2). In this case the required upward salt flux reduces the kinetic energy of the ocean and hence cannot, energetically speaking, drive a circulation.

Although salt and freshwater flux forcing is not likely to represent a source of energy, it can generate a stable stratification over much of the ocean, which in turn allows diffusion to transport fresh buoyant water downward, thus allowing for the maintenance of a diffusively driven over-turning circulation (via the second term in Equation (15)). We can estimate an upper bound for the energy source associated with molecular salt diffusion, given a maximum vertical salinity contrast. In an ocean driven by surface freshwater forcing, most of the ocean is expected to fill up with the saltiest water, leaving a relatively fresh surface layer in the region of net melting. The vertical salt contrast can then be approximately bounded by the global mean ocean salinity, as the deep ocean's salinity is expected to be near this mean value, while the surface salinity may be smaller but has to be positive. This gives an estimated upper bound for the global mean energy

source rate as

$$\epsilon \lesssim \frac{\kappa_S g \beta S}{H}. \tag{34}$$

For Snowball Earth, using $\kappa_S \sim 10^{-9}$ m^2 s^{-1}, $g = 10$ m s^{-2}, $\beta \sim 10^{-3}$ kg g^{-1}, $S \lesssim 70$ g kg^{-1}, and $H \gtrsim 2 \times 10^3$ m, we obtain $\epsilon \lesssim 3 \times 10^{-13}$ m^2 s^{-3}. For Europa, using $S \lesssim 100$ g kg^{-1}, $g = 1$ m s^{-2}, and $H \sim 10^5$ m, we obtain $\epsilon \lesssim 10^{-15}$ m^2 s^{-3}; and for Enceladus, with $g = 0.1$ m s^{-2}, $S \lesssim 30$ g kg^{-1}, and $H \gtrsim 1 \times 10^4$ m, we obtain $\epsilon \lesssim 3 \times 10^{-16}$ m^2 s^{-3}. For Snowball Earth and Europa, these upper bound estimates are at least 2 orders of magnitude lower than our estimates for the energy input from vertical heat flux (Table 2), suggesting that molecular diffusion even in the presence of a strong salt stratification is unlikely to be a major energy source. For Enceladus, vertical salt diffusion is also unlikely to be an important energy source although molecular diffusion may be important if the salinity is low enough for the thermal expansivity to be negative and if other potential mechanical energy sources (such as tides or librations) are negligible. In the presence of significant tidally driven turbulence, the tidally driven mixing effectively replaces the molecular diffusivity and can become a dominant energy source in all oceans. This will be discussed in the next section.

As for virtually all numerical simulations, the models of Zhu et al. (2017), Kang et al. (2020), Ashkenazy & Tziperman (2021), Kang et al. (2022), and Lobo et al. (2021) employ vertical diffusivities that are multiple orders of magnitude larger than the molecular value. In this case vertical diffusion acting against a statically stable stratification can drive a substantial circulation. This is illustrated in Figure 10 for a "salt-driven" Enceladus ocean simulation from Kang et al. (2022),[11] which uses a vertical diffusivity of $\kappa = 5 \times 10^{-3}$ m^2 s^{-1}. The primary source of mechanical energy in the simulations is associated with vertical diffusion of salt, which balances the energy sink associated with salt fluxes at the ice–ocean interface as well as the kinetic energy dissipation at the boundaries and in the ocean interior. However, as in the low-salinity Enceladus simulations of Zeng & Jansen (2021) discussed above, the large vertical diffusivities need to be interpreted as representing mixing by unresolved small-scale turbulence. In reality, this turbulent mixing requires a source of kinetic energy, and the mechanistic basis for this energy source must be established in order for the results of the simulations to be sound. In Earth's ocean today the source of energy for small-scale turbulent kinetic energy ultimately comes from winds and tides (e.g., Wunsch & Ferrari 2004). Surface wind stress is absent in globally ice-covered oceans, which leaves tides or librations as the most obvious source of turbulent kinetic energy in an ocean where buoyancy forcing is primarily due to salt fluxes at the ice–ocean interface.

5. Tides and Turbulent Mixing

5.1. Theory

Tidal forcing generates kinetic energy in the ocean (via the second term on the lhs of Equation (4)). The tidal perturbation potential is typically approximately vertically constant throughout the depth of the ocean, thus generating primarily barotropic

---

[11] The results shown here are from the simulation with a 3D geometry and intermediate salinity $S = 20$ g kg^{-1} in Kang et al. (2022).
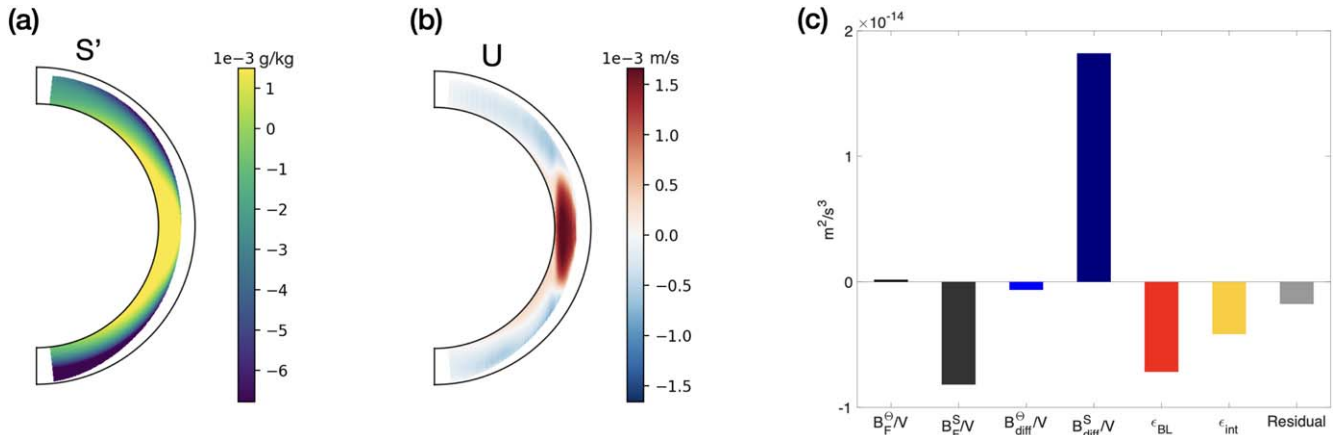
Figure 10. Results for a "salt-driven" Enceladus ocean simulation from Kang et al. (2022). Salt flux forcing from freezing and melting is prescribed at the bottom of an ice sheet that is thicker at the equator and thinner near the poles. The mean ocean salinity is 20 g kg^{-1}, which leads to a very small thermal expansivity, and the simulation does not include heating at the ocean floor. As a result, density gradients and energetics are dominated by the salinity and salt fluxes. (a) Snapshot of the salinity and (b) zonal velocity as a function of the depth and latitude. (c) Energy budget. From left to right are the energy sources and sinks (per unit volume) due to heat flux forcing at the boundaries ($\mathcal{B}_{\mathcal{F}}^{\Theta}/V$), salt flux forcing at the boundaries ($\mathcal{B}_{\mathcal{F}}^{S}/V$), vertical diffusion of heat ($\mathcal{B}_{\mathrm{diff}}^{\Theta}/V$), vertical diffusion of salt ($\mathcal{B}_{\mathrm{diff}}^{S}/V$), boundary-layer dissipation (ϵ_{BL}), and interior viscous dissipation (ϵ_{int}). The last bar shows the residual associated with nonequilibrium effects and errors in our offline calculation of the energy budgets.

(i.e., vertically constant) tides. In Earth's ocean these barotropic tidal waves are largely linear until they encounter shallow shelves, where the tidal amplitude increases and most of the tidal energy dissipation is assumed to occur (Wunsch & Ferrari 2004). The icy moons do not have shelf seas similar to Earth's ocean, although tidal dissipation may nevertheless be significantly enhanced in specific regions (e.g., Hay & Matsuyama 2019). Linear tides in the deep ocean do not contribute significantly to the transport of heat, salt, and other properties in the ocean, such that global models of Earth's ocean circulation can reproduce realistic large-scale circulations and tracer distributions without explicitly accounting for tides. However, it is possible that tidal waves on some icy moons become sufficiently nonlinear to lead to substantial rectified mean flows (e.g., Huthnance 1981; Brink 2011). As the current manuscript is focused on buoyancy-driven circulation, we will not further consider the possible role of rectified tidal flows here, but note that this remains a potentially important topic for further research.

Despite weak direct interactions with the large-scale flow, ocean tides can have an important effect on the large-scale circulation in the presence of a statically stable stratification (e.g., driven by freshwater fluxes at the ice–ocean interface). Barotropic tides interacting with a rough seafloor topography in the presence of a statically stable stratification can transfer their energy into baroclinic tides, i.e., internal waves that propagate both horizontally and vertically and can be associated with substantial vertical shears (e.g., MacKinnon et al. 2017 and references therein). These shears in turn can lead to instabilities and eventually the generation of turbulence within the water column. This pathway is believed to be one of the main drivers of 3D turbulence in Earth's deep ocean (Vic et al. 2019). Although most of the the turbulent kinetic energy is dissipated into heat, some fraction, usually denoted by the "mixing efficiency," Γ, is converted to potential energy via vertical mixing of the stratified water column:

$$\mathcal{B}^t = \int \overline{(w'b')^t} dV = -\int \Gamma \epsilon^t dV, \qquad (35)$$

where $-\mathcal{B}^t$ is the potential energy generation due to tidally driven turbulent mixing, $\overline{(w'b')^t}$ is the vertical buoyancy flux associated with tidally driven turbulence, ϵ^t is the tidally generated turbulent kinetic energy dissipation rate per unit mass, and $\Gamma \lesssim 0.2$ is the mixing efficiency (e.g., Peltier & Caulfield 2003).

The potential energy generated by turbulent mixing in a stratified ocean can then drive a large-scale circulation that converts the potential energy back to kinetic energy via a positive conversion $\overline{w}\overline{b}$ (where the overbars denote the large-scale circulation). If turbulent mixing is the dominant source of potential energy (i.e., when buoyancy gain and buoyancy loss from external forcing occur at approximately the same depth) the conversion $\overline{w}\overline{b}$ is, on average, approximately equal and opposite to the downward buoyancy flux associated with tidally driven turbulence:

$$\mathcal{B} \equiv \int wb\, dV = \int \overline{w}\overline{b}\, dV + \int \overline{(w'b')^t} dV \equiv \overline{\mathcal{B}} + \mathcal{B}^t \approx 0,$$

$$(36)$$

where $\overline{\mathcal{B}}$ is the kinetic energy generated (and ultimately dissipated) by the mean flow. The energy cycle can then be summarized as follows. Tides generate turbulent kinetic energy, a fraction of which is converted into large-scale potential energy via downward turbulent buoyancy flux (with the remainder being dissipated into heat). This potential energy can then be converted back to kinetic energy (and ultimately be dissipated) by the large-scale circulation. This mechanism requires a statically stable stratification such that turbulent mixing transports buoyancy downward. In the absence of a statically stable stratification, we still expect tidally driven turbulence to contribute to the mixing of properties, but we do not expect it to contribute to driving large-scale circulation.

In addition to tides, librations and injection of fluid through fissures in the ice or solid core may provide sources of kinetic energy. Librations are expected to play a similar role to tides, and as for tides, their effect on the large-scale circulation is expected to depend on their ability to generate turbulence in the

Table 1

Overview of Assumed Parameter Ranges for the Seafloor Heating Rate, Q, Gravitational Acceleration, g, Thermal Expansion Coefficient, α, Ocean Depth, H, and Coriolis Parameter, f, for Snowball Earth, Europa, and Enceladus. (The Sources are Cited in the Text.) Notice That the Uncertainties in Gravity and Rotation Rate are Comparatively Small and Hence Ignored Here

	Q (Wm^{-2})	g (ms^{-2})	α (K^{-1})	H (m)	Ω (s^{-1})
Snowball Earth	0.1	10	1×10^{-4}–2×10^{-4}	2×10^{3}–3×10^{3}	8×10^{-5}
Europa	0.02–0.1	1	1×10^{-4}–3×10^{-4}	5×10^{4}–1.5×10^{5}	2×10^{-5}
Enceladus	0.01–0.08	0.1	$< 1 \times 10^{-4}$	1×10^{4}–5×10^{4}	5×10^{-5}

Table 2

Overview of Estimates for Mechanical Energy Input (Per Unit Mass) Due to Thermal Forcing, $\epsilon = \mathcal{B}/H$, the Critical Length Scale Where Rotation is Expected to Become Important, $L_{\rm rot}$, the Convective Rossby Number for Rotating Convection, $\mathrm{Ro}_{\rm rc}$, and an Estimate of the Maximum Characteristic KE Energy (Assuming Small Interior Dissipation) of the Large-scale Geostrophic flow, E_g, for Snowball Earth, Europa, and Enceladus

	ϵ (m^2 s^{-3})	$L_{\rm rot}$(m)	$\mathrm{Ro}_{\rm rc}$	E_g(m^2 s^{-2})
Snowball Earth	2.5–5×10^{-11}	7–10	2–5×10^{-3}	10^{-4}–10^{-3}
Europa	5×10^{-13}–8×10^{-12}	8–30	1–8×10^{-4}	5×10^{-5}–3×10^{-3}
Enceladus	$\lesssim 2 \times 10^{-13}$	$\lesssim 1$	$\lesssim 1 \times 10^{-4}$	$\lesssim 10^{-4}$

ocean interior and on the presence of a statically stable stratification. Injection of water through fissures in the boundaries (which is not formally included in the global kinetic energy budget in Equation (4), where we assumed no-normal-flow boundary conditions) is likely to drive mechanical turbulence primarily in the vicinity of the boundaries, but strong jets emanating from the ice shell, as proposed by Kite & Rubin (2016), may play an important role in the dynamics of the upper ocean.[12] A full investigation of the effects of such jets is beyond the scope of this study, but remains an interesting subject for future research.

5.2. Application to Snowball Earth, Europa, and Enceladus

We begin by estimating the potential role of tidally driven turbulence in the Snowball Earth ocean. Although little is known about tidal energy dissipation during the Snowball Earth periods, the average tidal dissipation between the Precambrian and the present was likely somewhat smaller but of similar order of magnitude as the present-day value (Williams 2000; Green et al. 2017). The direct effect of the Snowball Earth ice sheet on tides was likely small (Wunsch 2016). For scaling purposes we therefore here assume a tidal energy input on the order of 10^{12} W, which is comparable to the present-day value of around 3.5×10^{12} W (Wunsch & Ferrari 2004). Assuming a mean ocean depth of about 2 km, an ocean area of 3.5×10^{14} m^2, and density $\rho_0 \approx 1000$ kg m^{-3}, the average tidal energy dissipation per unit mass is around $\epsilon^t \approx 10^{-9}$ m^2 s^{-3}, which is a little over an order of magnitude larger than the estimated energy input due to thermal forcing

(see Table 2). If a significant fraction of the dissipated tidal energy is dissipated in the stratified ocean interior and is relatively efficiently converted to potential energy (i.e., $\Gamma \gtrsim 10\%$) it thus may play a significant role in driving a large-scale ocean circulation. In particular, one may envision a scenario where freezing and melting at the ice–ocean interface combined with tidally driven turbulent mixing, which pushes the light fresh water into the ocean interior, can drive a significantly stronger large-scale ocean circulation than the thermal forcing alone. This scenario appears to be relevant for the interpretation of the simulation results by Ashkenazy et al. (2013) and Jansen (2016), although the turbulent vertical mixing in these simulations is parameterized with prescribed vertical diffusivities (i.e., $(\overline{w'b'})_t \rightarrow -\kappa \partial_z \bar{b}$) and is thus not constrained by tidal energy dissipation. The present analysis nevertheless suggests that the vertical mixing may be justifiable on energetic grounds given the expected tidally driven turbulence, although it would require that a significant fraction of the tidal energy is dissipated in the stratified ocean interior (as opposed to being highly localized in boundary layers where the stratification is vanishingly small) and is relatively efficiently converted to potential energy.

Tidal energy dissipation on Europa has been estimated from modeling to be on the order of 10^9–10^{11} W (Chen et al. 2014; Matsuyama et al. 2018; Hay & Matsuyama 2019). Assuming, as before, an ocean depth on the order of 10^5 m, an area of around 3×10^{13} m^2, and a density $\rho_0 \approx 1000$ kg m^{-3}, we estimate a tidal energy dissipation per unit volume of around $\epsilon^t \approx 3 \times 10^{-13}$–$3 \times 10^{-11}$ m^2 s^{-3}, which is between about 1 order of magnitude smaller to 2 orders of magnitude larger than the energy input by buoyancy forcing (see Table 2). Depending on the estimate for tidal energy dissipation, and the fraction of the dissipated tidal energy that is converted to potential energy, tidally driven turbulent mixing thus may or may not play a significant role in driving a large-scale ocean circulation on Europa. In particular, freezing and melting at the ice–ocean interface combined with tidally driven turbulent mixing may drive a significantly stronger large-scale ocean circulation then the thermal forcing alone, if, and only if, ocean tidal dissipation is near the upper end of these estimates and a large fraction of that energy contributes to vertical mixing against a stable stratification. A significant salt-driven circulation was found in

---

[12] For steady planar turbulent jets in an unstratified fluid, the peak mean flow speed has been found to decay with distance from the orifice as $U_{\max} \approx 2.5\sqrt{d/x}$, where d is the width of the slot from which the jet emanates and x is the distance (e.g., Gutmark & Wygnanski 1976). Turbulent flow speeds are about 20%–25% of this value. Kite & Rubin (2016) suggest that Enceladus' "tiger stripes" are associated with O(1 m) wide slots in which tidal forces generate O(1 m s^{-1}) jets. Assuming a neutral stratification, the results for planar turbulent jets would then suggest peak mean flows on the order of 10 cm s^{-1} and associated turbulent velocities on the order of a few cm s^{-1} to persist to a depth of a few hundred meters into the ocean. The relatively weak depth dependence ($U_{\max} \propto x^{-1/2}$) moreover indicates that weaker but significant flows may be penetrating much deeper, although results for steady jets are likely to become less applicable to the oscillatory jets proposed by Kite & Rubin (2016) at a greater depth. Stratification may further limit the penetration depth of turbulent jets.

the simulations of Ashkenazy & Tziperman (2021), although turbulent vertical mixing is parameterized with a prescribed Earth-like vertical diffusivity in the simulations and is not constrained by tidal energy dissipation. Better estimates of tidal energy dissipation in Europa's ocean are needed to determine whether such a large turbulent vertical diffusivity can be justified for stratified regions of Europa's ocean.

For Enceladus' ocean, energy dissipation associated with the eccentricity and obliquity tides has been estimated to be relatively small, with a total dissipation between 10 and 10^4 W suggested by Matsuyama et al. (2018) and Hay & Matsuyama (2019). More recently, Rovira-Navarro et al. (2023) argued that much larger tidal dissipation may occur in the presence of strong stratification and baroclinic tide resonances, although dissipation rates larger than 10^6 W remain unlikely for the expected range of stratifications. Tyler (2020) has argued that much larger dissipation rates are possible, accounting for virtually all of the observed $O(10^{10}$ W) heat flux, although the calculations generally predict the total dissipation in the ice–ocean system, and it is likely that most of the dissipation in the suggested scenarios would indeed occur in the ice sheet (see Beuthe 2016). Assuming that the most likely range for ocean tidal dissipation on Enceladus is $\sim$10–10^6 W, and using an average ocean depth of around 3×10^4 m and an area of around 5×10^{11} m^2, we find an average tidal energy dissipation rate anywhere between around $\epsilon^t \approx 7 \times 10^{-19}$–$7 \times 10^{-14}$ m^2 s^{-3}. The upper end of this range remains more than an order of magnitude smaller than the estimated maximum mechanical energy input via thermal forcing (see Table 2).

However, Enceladus' ocean may be more strongly affected by librations of the ice shell, which is decoupled from the solid interior (Thomas et al. 2016). It is not clear whether librations lead to relatively modest dissipation confined to the ice–ocean boundary layer, thus not contributing significantly to interior mixing, or whether the excitation of internal waves or elliptical instability (an instability that can break up elliptical stream-lines) can lead to relatively strong mixing throughout the depth of the ocean (Lemasquerier et al. 2017; Wilson & Kerswell 2018; Rekier et al. 2019; Soderlund et al. 2020). At the extreme end, Wilson & Kerswell (2018) argue that it is possible that all of the $O(10$ GW) of heating on Enceladus may be a result of librational dissipation, which, divided by the mass of Enceladus' ocean would give $\epsilon^t \sim 10^{-9}$ m^2 s^{-3}—many orders of magnitude larger than the possible mechanical energy input from thermal forcing. In this case it is likely that libration-driven turbulence would play the dominant role in ocean mixing. Narrowing down the large uncertainty in the energy dissipation rate associated with libration-driven turbulence will be key to constraining the turbulent diffusivity, which is an essential parameter in numerical simulations of Enceladus' ocean (Zeng & Jansen 2021; Kang et al. 2022).

6. Conclusions

Consideration of the sources and dissipation rates of kinetic energy provides useful constraints for the circulation of ice-covered oceans. In general, kinetic energy can be generated by tides or by conversion from potential energy, which in turn can be generated by heat and salt flux forcing. We here assumed an ocean in a statistically steady state in the sense that the mean tendencies of heat, salt, and kinetic energy are small. Relaxing this assumption—e.g., by allowing for an actively growing ice sheet where the heat loss through the ice sheet is much larger

than the heating from the core (as proposed by Roberts & Nimmo 2008) would require the inclusion of tendency terms in our budgets, which in turn would lead to a significantly less well-constrained problem.

A commonly assumed forcing consists of heating from the solid core balanced by heat loss through the ice sheet, which acts as a source of potential energy and can drive an ocean circulation, as long as the thermal expansivity of the water is positive. In the oceans of Snowball Earth, Europa, and Enceladus, the associated energy input, however, is orders of magnitude smaller than the wind energy input that dominantly drives the circulation in Earth's present-day ocean. We predict that the resulting thermally driven flows have flow speeds of at most a few cm s^{-1} and will be strongly affected by rotation (i.e., small Rossby numbers). Numerical simulations of thermally driven flows on icy moons, which typically use artificially large viscous dissipation and sometimes artificially large thermal forcing may misrepresent both energy sources and sinks by multiple orders of magnitude, which can lead to widely different and unrealistic levels of kinetic energy.

The salt fluxes associated with freezing and melting at the ice sheet boundary only provide a source of potential energy if freezing occurs under thinner ice than melting, which is unlikely in equilibrium where freezing and melting needs to be in balance with the ice flow. In the more likely scenario where melting on average occurs at a shallower depth than freezing, the salt flux forcing acts as a sink of potential energy. Vertical mixing, which can push the lighter fresh water into the interior, is then needed to drive a circulation. Molecular diffusion can in theory accomplish such mixing, but the associated energy source is likely to be relatively small. Much stronger turbulent mixing may be driven by tidal energy dissipation.

Ocean tides and librations may provide a key energy source for ocean turbulence. Current estimates indicate that tidally driven vertical mixing is likely to be important in a Snowball Earth ocean, and could possibly play a significant role on Europa, while librations may provide a key source of turbulent kinetic energy on Enceladus. However, the magnitude and spatial distribution of turbulence generated by tides and librations remains highly uncertain, which represents a major hurdle to better constrain the circulations of icy-world oceans. An improved understanding of ocean tides and librations on icy moons thus remains an important topic for future research.

Appendix
A Generalized Expression for the Energy Input from Buoyancy Forcing

To quantify the role of heat and salinity forcing on the vertical buoyancy flux, while fully accounting for nonlinearities in the equation of state, it is useful to introduce the dynamic enthalpy (Young 2010):

$$h^{\ddagger}(\Theta, S, z) = \int_z^0 \tilde{b}(\Theta, S, z') dz'. \tag{A1}$$

The dynamic enthalpy, $h^{\ddagger}$, is closely related to the potential energy, and indeed reduces to the well-known expression for the potential energy in the limit of an equation of state with no explicit depth dependence (i.e., $b = \tilde{b}(\Theta, S)$), where $h^{\ddagger} \to bz$.

The evolution equation for $h^{\ddagger}$ is

$$\frac{Dh^{\ddagger}}{Dt} = -wb + \dot{\Theta}\partial_{\Theta}h^{\ddagger} + \dot{S}\partial_S h^{\ddagger}, \tag{A2}$$

where $\dot{\Theta} \equiv D\theta/Dt$ and $\dot{S} \equiv DS/Dt$ are given by Equations (6) and (7), respectively.

Integrating globally and assuming the global enthalpy budget to be in equilibrium, we can relate the globally integrated vertical advective buoyancy flux, $\mathcal{B}$, which provides a source of KE, to the thermal and salinitiy forcing, $\dot{\Theta}$ and $\dot{S}$:

$$\mathcal{B} \equiv \int wb \, dV = \int (\dot{\Theta}\partial_\Theta h^{\ddagger} + \dot{S}\partial_S h^{\ddagger}) dV. \quad (A3)$$

Defining

$$\widehat{g\alpha}(\Theta, S, z) \equiv \frac{1}{-z}\partial_\Theta h^{\ddagger} = \frac{1}{-z}\int_z^0 g\alpha(\Theta, S, z')dz' \quad (A4)$$

and

$$\widehat{g\beta}(\Theta, S, z) \equiv \frac{1}{-z}\partial_S h^{\ddagger} = \frac{1}{-z}\int_z^0 g\beta(\Theta, S, z')dz', \quad (A5)$$

we can write Equation (A3) as

$$\begin{aligned}
\mathcal{B} &= -\int (\dot{\Theta}\widehat{g\alpha}z + \dot{S}\widehat{g\beta}z)dV \\
&= -\int \kappa(\nabla^2\Theta\,\widehat{g\alpha}z + \nabla^2 S\,\widehat{g\beta}z)dV \\
&= -\int \kappa(\nabla\cdot(\nabla\Theta\,\widehat{g\alpha}z) - \nabla\Theta\cdot\nabla(\widehat{g\alpha}z) \\
&\quad + \nabla\cdot(\nabla S\,\widehat{g\beta}z) - \nabla S\cdot\nabla(\widehat{g\beta}z))dV \\
&= \int \frac{\mathcal{Q}_{\text{top}}}{\rho c_p}\widehat{g\alpha}z_{\text{top}}dA - \int \frac{\mathcal{Q}_{\text{bot}}}{\rho c_p}\widehat{g\alpha}z_{\text{bot}}dA \\
&\quad + \int \mathcal{S}_{\text{top}}\widehat{g\beta}z_{\text{top}}dA - \int \mathcal{S}_{\text{bot}}\widehat{g\beta}z_{\text{bot}}dA \\
&\quad + \int g\kappa(\alpha\partial_z\Theta + \beta\partial_z S)dV \\
&\quad + \int z\kappa(\nabla_h(\widehat{g\alpha})\cdot\nabla_h\Theta + \nabla_h(\widehat{g\beta})\cdot\nabla_h S)dV. \quad (A6)
\end{aligned}$$

Equation (A6) allows us to relate the globally integrated advective upward buoyancy flux (and hence the associated KE generation) to the heat and salt fluxes through the boundaries (the first four terms on the rhs of Equation (A6)), reduced by the diffusive buoyancy flux (the fifth term on the rhs of Equation (A6)). The last term in Equation (A6) captures the effect of buoyancy sources or sinks that arise from horizontal diffusive mixing of Θ and S due to the nonlinearity in the equation of state (the cabbeling effect).

The potential role of the cabbeling term in Equation (A6) can be illustrated by considering again the example of Section 3.3, which may resemble the conditions on Enceladus, assuming a relatively low salinity for the latter. That is we assume a stratified layer with negative thermal expansion coefficient above a convective deep layer with weakly positive thermal expansion coefficient. For illustrative purposes, let us assume the upper and lower boundaries to be horizontal, and the bottom and surface heat fluxes to be spatially uniform; we also ignore radial variations in the surface area, such that $Q_{\text{top}} = Q_{\text{bot}} \equiv Q$, as well as vertical variations in gravity. As variations in the thermal expansion coefficient are primarily due to differences in the temperature, we moreover neglect the direct depth dependence of $\tilde{b}$ and assume that variations in salinity are small, such that $\widehat{g\alpha} = g\alpha(\theta)$. In this case,

Equation (A6) simplifies to

$$\begin{aligned}
\mathcal{B} &= \frac{gQ}{\rho c_p}\int (\alpha(\Theta_{\text{top}})z_{\text{top}} - \alpha(\Theta_{\text{bot}})z_{\text{bot}})dA \\
&\quad + \int g\kappa\alpha(\Theta)\partial_z\Theta \, dV + \int gz\kappa\partial_\Theta\tilde{\alpha}|\nabla_h\Theta|^2 dV,
\end{aligned}$$

where we used that $\nabla_h\alpha \cdot \nabla_h\Theta = \partial_\Theta\alpha|\nabla_h\Theta|^2$. The last term can now be associated with the diffusive destruction of temperature variance, which leads to a buoyancy source if $\partial_\Theta\alpha > 0$ (amounting to a positive curvature in $b(\theta)$).

Notice that the magnitude (and potentially the sign) of the first and last terms in Equation (A7) depend on the choice of reference level. For instance, setting $z_{\text{bot}} = 0$ and $z_{\text{top}} = H$, where H is the depth of the ocean (which we assume to be constant with flat upper and lower boundaries), we find

$$\begin{aligned}
\mathcal{B} &= \frac{gQH}{\rho c_p}\int \alpha(\Theta_{\text{top}})dA \\
&\quad + \int g\kappa\alpha(\Theta)\partial_z\Theta \, dV + \int_0^H gz\kappa\partial_\Theta\alpha|\nabla\Theta|^2 dV. \quad (A7)
\end{aligned}$$

Defining the reference level instead such that $z_{\text{top}} = 0$ and $z_{\text{bot}} = -H$, we obtain

$$\begin{aligned}
\mathcal{B} &= \frac{gQH}{\rho c_p}\int \alpha(\Theta_{\text{bot}})dA \\
&\quad + \int g\kappa\alpha(\Theta)\partial_z\Theta \, dV + \int_{-H}^0 gz\kappa\partial_\Theta\alpha|\nabla\Theta|^2 dV. \quad (A8)
\end{aligned}$$

The first term differs dramatically in the two equations, as $\alpha(\Theta_{\text{top}}) < 0$ while $\alpha(\Theta_{\text{bot}}) > 0$. This difference is compensated by the last term, which also changes sign, as $z > 0$ in Equation (A7) and $z < 0$ in Equation (A8). The last term in Equation (A6) hence can be of leading-order importance if variations in the thermal (or haline) expansion coefficient are large. As this term cannot be predicted based on knowledge of the boundary conditions alone, this most general formulation is hence less immediately useful as a predictor of flow energetics. However, if horizontal temperature variations are relatively small, Equation (14) remains a useful approximation and allows us to estimate the kinetic energy input without explicit consideration of diffusive variance destruction.

ORCID iDs

Wanying Kang https://orcid.org/0000-0002-4615-3702
Edwin S. Kite https://orcid.org/0000-0002-1426-1186
Yaoxuan Zeng https://orcid.org/0000-0002-2624-8579

References

Adcroft, A., Anderson, W., Balaji, V., et al. 2019, JAMES, 11, 3167
Anderson, J., Schubert, G., Jacobson, R., et al. 1998, Sci, 281, 2019
Ashkenazy, Y., Gildor, H., Losch, M., et al. 2013, Natur, 495, 90
Ashkenazy, Y., & Tziperman, E. 2016, JCli, 29, 869
Ashkenazy, Y., & Tziperman, E. 2021, NatCo, 12, 6376
Aubert, J., Brito, D., Nataf, H.-C., Cardin, P., & Masson, J.-P. 2001, PEPI, 128, 51
Beuthe, M. 2016, Icar, 280, 278
Bire, S., Kang, W., Ramadhan, A., Campin, J.-M., & Marshall, J. 2022, JGRE, 127, e2021JE007025
Brenner, S., Rainville, L., Thomson, J., Cole, S., & Lee, C. 2021, JGRC, 126, e2020JC016977
Brink, K. H. 2011, JMR, 69, 483

Čadek, O., Tobie, G., Van Hoolst, T., et al. 2016, GeoRL, 43, 5653
Cardin, P., & Olson, P. 1994, PEPI, 82, 235
Carr, M. H., Belton, M. J., Chapman, C. R., et al. 1998, Natur, 391, 363
Chen, E., Nimmo, F., & Glatzmaier, G. 2014, Icar, 229, 11
Chen, Y., Zhang, F., Green, B. W., & Yu, X. 2018, MWRv, 146, 287
Choblet, G., Tobie, G., Sotin, C., et al. 2017, NatAs, 1, 841
Des Marais, D. J., Nuth, J. A., III, Allamandola, L. J., et al. 2008, AsBio, 8, 715
Egbert, G. D., Ray, R. D., & Bills, B. G. 2004, JGRC, 109, C03003
Fernando, H. J., Chen, R.-R., & Boyer, D. L. 1991, JFM, 228, 513
Gastine, T., Wicht, J., & Aubert, J. 2016, JFM, 808, 690
Gissinger, C., & Petitdemange, L. 2019, NatAs, 3, 401
Glein, C. R., Postberg, F., & Vance, S. D. 2018, Enceladus and the Icy Moons of Saturn (Tucson, AZ: Univ. Arizona Press), 39
Green, J., Huber, M., Waltham, D., Buzan, J., & Wells, M. 2017, E&PSL, 461, 46
Gutmark, E., & Wygnanski, I. 1976, JFM, 73, 465
Hay, H. C., & Matsuyama, I. 2019, Icar, 319, 68
Hemingway, D., Iess, L., Tajeddine, R., & Tobie, G. 2018, Enceladus and the Icy Moons of Saturn (Tucson, AZ: Univ. Arizona Press), 57
Hendrix, A. R., Hurford, T. A., Barge, L. M., et al. 2019, AsBio, 19, 1
Hoffman, P. F., Abbot, D. S., Ashkenazy, Y., et al. 2017, SciA, 3, e1600983
Hughes, G. O., & Griffiths, R. W. 2008, AnRFM, 40, 185
Hussmann, H., & Spohn, T. 2004, Icar, 171, 391
Huthnance, J. 1981, JFM, 102, 367
Jansen, M. F. 2016, JPO, 46, 1917
Jones, H., & Marshall, J. 1993, JPO, 23, 1009
Kang, W., Bire, S., Campin, J.-M., et al. 2020, arXiv:2008.03764
Kang, W., Mittal, T., Bire, S., Campin, J.-M., & Marshall, J. 2022, SciA, 8, eabm4665
Kite, E. S., & Rubin, A. M. 2016, PNAS, 113, 3972
Kivelson, M. G., Khurana, K. K., Russell, C. T., et al. 2000, Sci, 289, 1340
Korenaga, J. 2008, RvGeo, 46, RG2007
Lemasquerier, D., Grannan, A., Vidal, J., et al. 2017, JGRE, 122, 1926
Lobo, A. H., Thompson, A. F., Vance, S. D., & Tharimena, S. 2021, NatGe, 14, 185

MacKinnon, J. A., Zhao, Z., Whalen, C. B., et al. 2017, BAMS, 98, 2429
Matsuyama, I., Beuthe, M., Hay, H. C., Nimmo, F., & Kamata, S. 2018, Icar, 312, 208
Maxworthy, T., & Narimousa, S. 1994, JPO, 24, 865
Melosh, H., Ekholm, A., Showman, A., & Lorenz, R. 2004, Icar, 168, 498
Nakajima, A., Ida, S., Kimura, J., & Brasser, R. 2019, Icar, 317, 570
Nimmo, F., & Pappalardo, R. 2016, JGRE, 121, 1378
Paparella, F., & Young, W. 2002, JFM, 466, 205
Peltier, W., & Caulfield, C. 2003, AnRFM, 35, 135
Postberg, F., Khawaja, N., Abel, B., et al. 2018, Natur, 558, 564
Rekier, J., Trinh, A., Triana, S. A., & Dehant, V. 2019, JGRE, 124, 2198
Roberts, J. H., & Nimmo, F. 2008, Icar, 194, 675
Rovira-Navarro, M., Matsuyama, I., & Hay, H. C. C. 2023, PSJ, 4, 23
Ruiz, J. 2005, Icar, 177, 438
Sandström, J. W. 1908, Ann. Hydrodyn. Mar. Meteorol., 36, 6
Sen, A., Scott, R. B., & Arbic, B. K. 2008, GeoRL, 35, L09606
Smagorinsky, J., Manabe, S., & Holloway, J. L. 1965, MWRv, 93, 727
Soderlund, K., Schmidt, B., Wicht, J., & Blankenship, D. 2014, NatGe, 7, 16
Soderlund, K. M. 2019, GeoRL, 46, 8700
Soderlund, K. M., Kalousová, K., Buffo, J. J., et al. 2020, SSRv, 216, 1
Thomas, P., Tajeddine, R., Tiscareno, M., et al. 2016, Icar, 264, 37
Tyler, R. H. 2020, Icar, 348, 113821
Vallis, G. K. 2006, Atmospheric and Oceanic Fluid Dynamics (Cambridge: Cambridge Univ. Press), 745
Vance, S. D., Panning, M. P., Stähler, S., et al. 2018, JGRE, 123, 180
Vic, C., Garabato, A. C. N., Green, J. M., et al. 2019, NatCo, 10, 1
Waite, J. H., Glein, C. R., Perryman, R. S., et al. 2017, Sci, 356, 155
Williams, G. E. 2000, RvGeo, 38, 37
Wilson, A., & Kerswell, R. R. 2018, E&PSL, 500, 41
Wunsch, C. 2016, Icar, 274, 122
Wunsch, C., & Ferrari, R. 2004, AnRFM, 36, 281
Yang, J., Jansen, M. F., Macdonald, F. A., & Abbot, D. S. 2017, Geo, 45, 615
Young, W. R. 2010, JPO, 40, 394
Zeng, Y., & Jansen, M. F. 2021, PSJ, 2, 151
Zhu, P., Manucharyan, G. E., Thompson, A. F., Goodman, J. C., & Vance, S. D. 2017, GeoRL, 44, 5969